TÉCNICO LISBOA

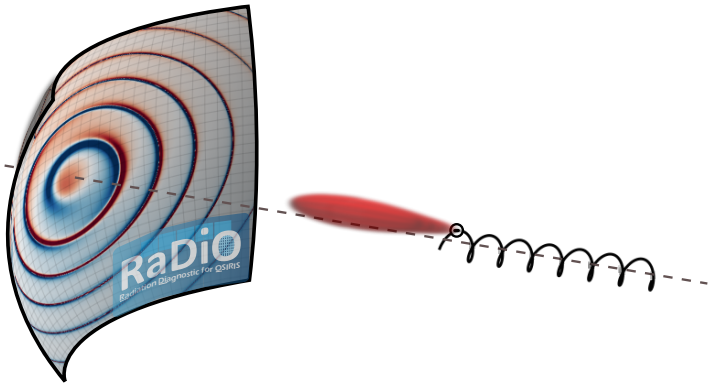

Modelling ultra-high frequency x-ray emission in particle in cell codes

Miguel José Ferreira Pardal

Thesis to obtain the Master of Science Degree in

Engineering Physics

Supervisors: Prof. Jorge Miguel Ramos Domingues Ferreira Vieira
Prof. Ricardo Parreira de Azambuja Fonseca

Examination Committee

Chairperson: Prof. João Pedro Saraiva Bizarro
Supervisor: Prof. Jorge Miguel Ramos Domingues Ferreira Vieira
Members of the Committee: Prof. Marta Leitão Mota Fajardo
Dr. Joana Luís Martins

October 2018

Dedicated to someone special...

Resumo

Os processos de radiação em plasmas são de extrema relevância num vasto número de áreas desde a astrofísica à microscopia. Esses processos estão geralmente associados ao movimento de muitos electrões, onde os efeitos colectivos de plasma podem ser importantes. Deste modo, a compreensão desses processos requer usualmente modelação numérica e em particular, os códigos Particle-In-Cell conseguem descrever com precisão o movimento de cada partícula, no entanto, apresentam limitações a captar a radiação por ela emitida, dada a diferença entre as escalas temporais do movimento da partícula e da radiação emitida. Actualmente os diagnósticos de radiação são apenas capazes de capturar as propriedades espectrais da luz emitida. Este trabalho descreve um novo diagnóstico de radiação que captura as propriedades espacio-temporais da radiação, potencialmente úteis na identificação de cenários astrofísicos ou no aperfeiçoamento das fontes de radiação.

O algoritmo implementado é ideal para descrever a radiação de muitas partículas e foi totalmente integrado no código PIC OSIRIS, estando agora pronto para ser aplicado a qualquer cenário de emissão de radiação. Este algoritmo permite que o detector tenha uma resolução temporal arbitrariamente alta sem afetar significativamente a carga computacional. Mostra-se que a ferramenta recupera os espectros teóricos para cenários de emissão de radiação bem conhecidos, com desempenho paralelo satisfatório em alguns dos maiores supercomputadores do mundo e foi usada para calcular o perfil espacio-temporal da radiação de betatrão em aceleradores de plasma. As implicações do uso de macropartículas na simulação também são estudadas, propondo-se um método para recuperar os resultados laboratoriais.

Palavras-chave: Radiação, Plasma, Computação Paralela, Simulação, Detector

Abstract

Radiation processes in plasma are of extreme relevance for a vast number of fields ranging from astrophysics to small scale microscopy. These processes are usually associated with the motion of many individual electrons, where collective plasma effects can be important, thus, he understanding of these processes often requires numerical modelling. In particular, Particle In Cell codes are able to accurately describe the motion of individual particles but fail to capture the radiation due the difference between the temporal scales of the motion of the particles and the emitted radiation. Current radiation emission diagnostics can capture spectral properties of the emitted light. This work, describes a new radiation diagnostic that captures the unexplored spatiotemporal properties of radiation, potentially useful in the discovery of specific astrophysical scenarios or the enhancement of radiation sources.

The algorithm is ideal to describe the radiation from many particles and has been fully integrated into the particle-in-cell code OSIRIS, being now ready to be applied to any radiation emission scenario. This algorithm allows the detector to have an arbitralily high temporal resolution without significantly affecting the computational load. The tool is shown to recover the theoretical spectra for well-known scenarios of radiation emission with decent parallel performance in some of the world's largest supercomputers and was used to compute the spatiotemporal profile of betatron radiation in plasma accelerators. The implications of the use of macroparticles in the simulation are also studied and a method to recover the laboratory results is proposed.

Keywords: Radiation, Plasma, Parallel Computing, Simulation, Detector

Contents

List of Tables

List of Figures

Acronyms

CIC Cloud in Cell. 44

DMP Distributed Memory Processor. 15

GoLP Group of Lasers and Plasmas. 6, 8

HHG High Harmonic Generation. 2, 50

IST Instituto Superior Técnico. 3, 32

LWFA Laser Wakefield Acceleration. 35, 36

MPI Message Passing Interface. 14, 15

OAM Orbital angular momentum. xiii, 1, 2, 8

PIC Particle In Cell. 2–4, 6, 7

PWFA Plasma Wakefield Acceleration. 36, 37

SMP Shared Memory Processor. 15

UCLA University of California, Los Angeles. 3

Chapter 1

Introduction

1.1 Motivation

From the creation of sources of X-rays capable of probing nanoscale structures here on earth, to the mysterious gamma-ray bursts, whose properties can be studied through the structure of the radiation we receive, high-frequency radiation emission has puzzled the human mind for a long time, as it provides critical insights into remote astrophysical phenomena that cannot be reached otherwise. Usually, these observations rely on a spectral analysis of the light coming from far away. This methodology has led to significant discoveries and motivated the development of theoretical and numerical models [1].

Nevertheless, the interest in spatiotemporal features which can be frequency independent (*e.g.* spatial chirp or Orbital angular momentum (OAM) [2], has been increasing in recent years. One interesting example is the radiation emitted by rapidly rotating black holes which may contain a specific spatiotemporal signature [3]. Consequently, measuring the OAM of incoming light from the sky may provide new evidences for such structures. While it may be possible to retrieve such information from spectral properties like the phase (Figure 1.1), a spatiotemporal diagnostic capable of providing these results directly is clearly more desirable.

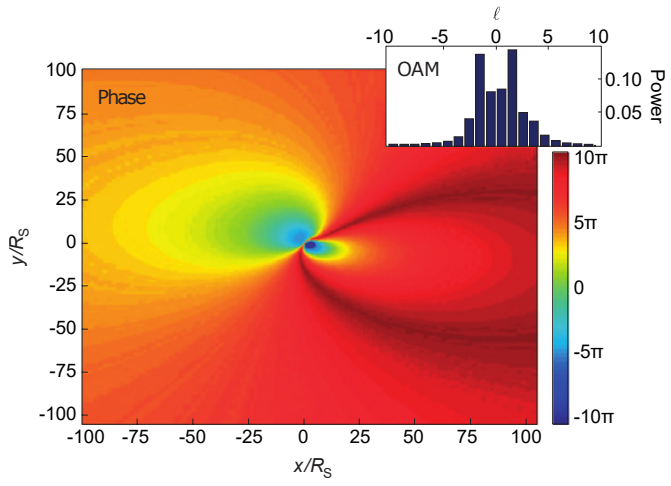

Figure 1.1: Phase variation and Orbital angular momentum spectrum of radiation emitted at the equatorial plane of a rapidly rotating black hole, as seen by an infinitely remote observer with an angle of 45º. Taken from Tamburini et al. [3].

However, black holes are only a small part of all the matter present in the universe. In fact recent estimates predict that 99% of the known universe is in plasma state [4], therefore, understanding radiation emission mechanisms in plasmas is crucial to the study of astrophysical observations.

Despite the strong interest in light from outer space, radiation emission also plays a major role here on earth. In fact, since their discovery, X-rays have found their place in a vast number of applications, for example, in high-resolution microscopy [5] where spatiotemporally structured beams help breaking the diffraction limit. In recent years, most of these applications have developed the need for ultra intense X-ray beams, like the ones generated by synchrotrons or free electron lasers [6]. This can be a major obstacle as these sources are usually extremely costly and large machines.

To reduce the size and the cost of conventional devices, there have been some substantial efforts in developing compact plasma based light sources [7, 8]. Relativistic plasma waves, driven by ultra intense laser and particle beams, provide strong fields that bend the trajectory of relativistic beams therefore generating strong bursts of the so-called betatron radiation [9].

Another approach relies on High Harmonic Generation (HHG), where short intense laser pulses interact with a target (solid, gaseous or plasma). Like in astrophysics, most of the work done in this field was focused on the spectral properties and recently its efficiency has been shown to depend on the OAM of the incident pulse [10]. Thus, understanding spatiotemporal behaviour of X-ray emission in plasmas is absolutely necessary for next generation X-ray sources.

1.2 Particle in Cell Simulation

The processes behind radiation emission in astrophysics or compact plasma accelerators result from many body interactions, are strongly non-linear, and involve relativistic effects, such that purely theoretical models are not available. Plasma simulations are thus crucial to validate theoretical models and explore all the processes self-consistently, to explain observational and experimental data, and also to design new plasma based light sources.

Particle In Cell (PIC) codes have been used since the 1950s to simulate the behaviour of plasmas [11] and are one of the most successful tools for modeling plasma accelerators and light sources, allowing for simulations without physical approximations to the extent where quantum mechanical and gravitational processes can be neglected. PIC simulation has been essential in cutting-edge fields such as plasma accelerators, plasma astrophysics and advanced laser-based fusion concepts [8].

A plasma is a system of many (N_p) particles that interact via electromagnetic forces, therefore, the most natural way of simulating it would be to calculate each interaction individually in a strategy known as particle-particle simulation. However, this is not feasible as the computational cost scales as N_p^2 (each of the N_p particles has $N_p - 1$ forces acting on it). Particle in Cell simulation is an excellent alternative, having been, in fact, the standard method for particle simulation of plasmas since its original proposal by Dawson [11], as it is very efficient for many-particle systems that interact through fields.

PIC simulation avoids the previous problem by making the particles interact through the electromagnetic fields discretized in a grid. The fields are calculated self-consistently in each time step from the

current density, through Maxwell's equations, described below:

$$\frac{\partial \mathbf{E}}{\partial t} = c\nabla \times \mathbf{B} - 4\pi \mathbf{j}, \qquad \frac{\partial \mathbf{B}}{\partial t} = -c\nabla \times \mathbf{E} \qquad \text{(cgs units)}, \tag{1.1}$$

where $\mathbf{E}$ is the electric field, $\mathbf{B}$ is the magnetic field, $\mathbf{j}$ is the electric current, and c is the speed of light.

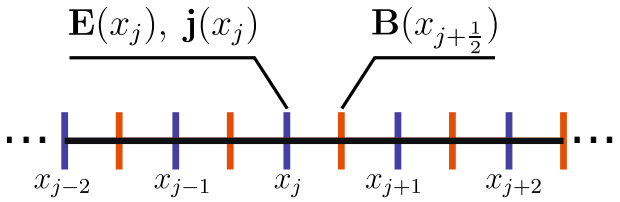

Figure 1.2: Illustration of the one-dimensional Yee scheme. The current $\mathbf{j}$ grid is aligned with the E-field grid.

The curl is calculated with a finite-difference approximation, and therefore, the electric and magnetic field are usually arranged in a Yee scheme [12] in order to obtain higher robustness and accuracy. This scheme corresponds to shifting the magnetic field grid (with respect to the electric field grid), so that each electric field point falls midway between two magnetic field points, as shown in Figure 1.2. Thus, Maxwell's equations are discretized in a staggered grid that ensures space and time centered calculations. Higher order schemes can also be constructed but the one developed by Yee provides a standard algorithm that forms the basis for more complex numerical approaches.

The current density is, in turn, obtained by advancing the particles using the relativistic form of the Lorentz force, shown below, where $\mathbf{u}$ is the velocity of the particle, $\dot{\mathbf{u}}$ is the acceleration of the particle and γ is the Lorentz factor, given by $\gamma = 1/\sqrt{1 + |\mathbf{u}|^2/c^2}$, with the so called Boris pusher [13].

$$\dot{\mathbf{u}} = \frac{q}{m}\left(\mathbf{E} + \frac{1}{c}\frac{\mathbf{u}}{\gamma} \times \mathbf{B}\right). \tag{1.2}$$

The field values at the particle's position come from an interpolation of the grid values at the previous time step. Therefore, PIC simulation consists in a loop (Figure 1.3) that advances every particle with self-consistently calculated fields in a computationally efficient, easily parallelizable, way. The amount of operations needed for each time step scales as $N_p + N_g$, where N_p is once again the number of particles and N_g is the number of grid points, which leads to major reductions in computation time when compared to particle-particle simulations.

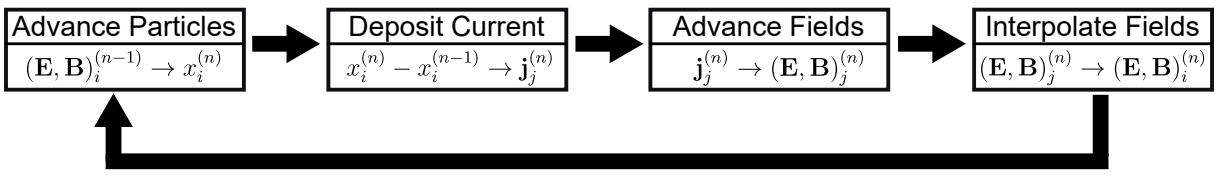

Figure 1.3: Particle in cell simulation loop. The i index is associated with particle numbering ($i = 1, 2, ...N_p$), whereas the j index is associated with grid position ($j = 1, 2, ...N_g$)

Most PIC codes use a system of normalized units that avoids multiplication by constants like the electron's mass m_e or the speed of light c, which increases performance and accuracy significantly. In particular, OSIRIS [13], a massively parallel fully relativistic PIC code developed in collaboration between IST and UCLA, uses the normalization system presented in Table 1.1, where the subscript p refers to

plasma quantities, such as the plasma frequency, ω_p or the plasma density, n_p.

Table 1.1: Normalization factors for OSRIS. The apostrophe denotes the normalized quantity. q_e is the electron's charge.

Quantity	Normalization
Length	$x' = x \cdot \omega_p/c$
Time	$t' = t \cdot \omega_p$
Charge	$q' = q/q_e$
Density	$n' = n/n_p$
Velocity	$v' = v/c$
Momenta	$p' = p/m_e c$
Electric Field	$E' = q_e/m_e \omega_p c$

Despite their efficiency, the run time of PIC codes still depends strongly on the number of grid points, which means that spatial (and consequently, temporal) resolution is a bottleneck of PIC simulation. In fact, simulating high frequency radiation processes is usually unfeasible given the disparity between the temporal and spatial scales associated with radiation processes. As illustrated by Figure 1.4 the temporal distance between two consecutive photons is given by $dt_{rad} = dt(1 - v_p/c) \simeq dt/2\gamma^2$, with dt being the temporal distance between emissions. Therefore, the frequency of the emitted radiation is at least $2\gamma^2$ times larger than the typical frequency of the radiation emission processes, which in the case of a relativistic particle ($\gamma \sim 100$) results in several orders of magnitude of difference between temporal scale of the radiation and its emission process. It is also important to note that the resolution should not be increased indefinitely as resolving time steps smaller than $dt/2\gamma^2$ will generate non-physical information.

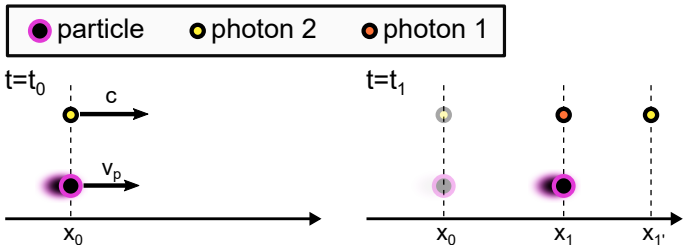

Figure 1.4: Illustration of radiation emission. The particle located at x_0 emits photon 1 at $t = t_0$. As the photon travels at c, in the next time step it will have traveled an extra $dt(\mathrm{c} - v_p)$ than the particle, which emits a second photon at $t = t_1$.

Thus, in order for the PIC simulation to self-consistently calculate ultra-high frequency radiated fields, a very high resolution would be required which would render such simulations unfeasible. For example, a 3D simulation of radiation emission by Thomson Scattering [14] that usually takes $\sim 10^4$ core hours would require about 10^{12} core hours in order to capture the full spectrum of radiation. That is the main reason why PIC codes do not retain the high frequency radiation emitted at wavelengths much shorter than the scale length of the plasma structures, despite making no physical approximations. Consequently, so far, none of the major PIC codes have a radiation functioning diagnostic able to capture the spatiotemporal properties of ultra-high frequency radiation emitted in the plasma and the spatiotemporal structure of such waves is remains largely unexplored and new strategies are required.

1.3 Radiation emission by moving charges

Whenever a charged particle is subject to acceleration, it emits electromagnetic radiation. This phenomenon can be modeled mathematically through the Liénard-Wiechert potentials, ϕ and $\mathbf{A}$, which give the classical electrodynamics description of the electromagnetic field for a moving particle with electric charge q_e [15].

The Liénard-Wiechert potentials can be derived by solving the covariant form of the inhomogeneous wave equation, $\Box A^\mu = (4\pi/c)J^\mu$ (cgs), using causal Green functions, where $\Box$ is the *D'Alembert* operator, $A^\mu = (\phi, \mathbf{A})$ and $J^\mu = (c\rho, \mathbf{J})$ are respectively the 4-vector potential and the 4-vector current, ρ is the charge density, and c the speed of light. From these potentials we can retrieve, for example, the angular and frequency distribution of the emitted radiation intensity $d^2I/d\Omega d\omega$:

$$\frac{d^2I}{d\omega d\Omega} = \frac{q_e^2}{4\pi^2 c}\left|\int_{-\infty}^{\infty} \frac{\mathbf{n}\times[(\mathbf{n}-\boldsymbol{\beta})\times\dot{\boldsymbol{\beta}}]}{(1-\boldsymbol{\beta}\cdot\mathbf{n})^2} e^{i\omega(t_{\text{ret}}-\frac{\mathbf{n}\cdot\mathbf{r}}{c})} dt_{\text{ret}}\right|^2 . \tag{1.3}$$

According to this equation, this distribution depends on the direction of observation, $\mathbf{n}$, the velocity and acceleration of the particle, $\boldsymbol{\beta}$ and $\dot{\boldsymbol{\beta}}$, as well as the position vector of the particle $\mathbf{r}$, which are all evaluated in the retarded time of emission, t_{ret}, as displayed in Figure 3.9. It is possible to deduce key properties of radiation emission from Equation (1.3) [16]:

- The term $(1-\boldsymbol{\beta}\cdot\mathbf{n})^{-2}$ inside the integrand grows when the direction of the particle's velocity, $\boldsymbol{\beta}$, approaches the direction of observation, $\mathbf{n}$, so radiation is mostly emitted in the direction the particle is traveling.

- The term $\mathbf{n}\times[(\mathbf{n}-\boldsymbol{\beta})\times\dot{\boldsymbol{\beta}})]$ grows with the acceleration, in general, and is larger when the acceleration is perpendicular to the velocity, so in terms of radiation emission for a relativistic particle traveling in the longitudinal direction, transverse acceleration is more efficient than longitudinal acceleration.

- If the leftmost part of the integrand oscillates at a given constant frequency ω_e (Figure 3.9), the integral is larger when the phase term oscillates at frequencies close to ω_e or its harmonics and the frequency distribution of the emitted radiation intensity would be composed of a set of peaks.

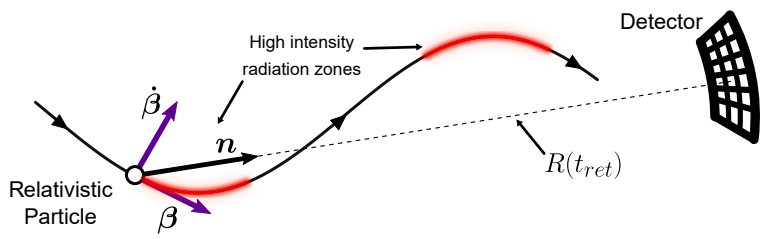

Figure 1.5: Illustration of the geometry of the radiation emission process and relevant quantities. The relativistic particle follows a sinusoidal trajectory. Higher intensity is obtained with transverse acceleration.

Despite capturing the spectral properties of the radiation, Equation (1.3) cannot be used directly to infer the spatiotemporal features of the radiation emitted by moving charges, which can be accessed

by the calculation calculation of the electric and magnetic fields of the radiation in space and time [15], given by:

$$\mathbf{E}(\mathbf{x},t) = \underbrace{e\left[\frac{\mathbf{n}-\boldsymbol{\beta}}{\gamma^2(1-\boldsymbol{\beta}\cdot\mathbf{n})^3R^2}\right]_{\text{ret}}}_{\text{A}} + \underbrace{\frac{e}{c}\left[\frac{\mathbf{n}\times[(\mathbf{n}-\boldsymbol{\beta})\times\dot{\boldsymbol{\beta}})]}{(1-\boldsymbol{\beta}\cdot\mathbf{n})^3R}\right]_{\text{ret}}}_{\text{B}}, \qquad \mathbf{B}(\mathbf{x},t) = [\mathbf{n}\times\mathbf{E}]_{\text{ret}}\,. \tag{1.4}$$

All quantities must be evaluated at the time of emission, t_{ret}. Additionally, the radiated electric field has two separate components which are usually called *velocity fields* (A) and *acceleration fields* (B). As the velocity fields decay with R^2, they are often neglected under the assumption that the detector is far enough to allow $R^2 \gg R$.

1.4 State of the Art

Post processing and run-time tools have been a successful approach, using stored trajectories to describe the radiation in the Fourier space [17, 18]. Even so, these tools do not describe the spatiotemporal properties of the radiation.

In recent years, several efforts have been made aiming to describe the spectral and spatiotemporal properties of the radiation emitted in PIC simulations. One way to do so is to use the particle's trajectory to compute such properties. This is the principle behind post processing tools such as JRad [17], which is described below.

1.4.1 Post processing radiation tools

Currently, there are several radiation post-processing tools available throughout the community, a remarkable example is JRad. JRad is a massively parallel post-processing radiation code developed at GoLP that captures the power and spectral aspects of radiation by solving Equation (1.3). This code exploits the particle tracking capabilities of the OSIRIS framework and uses the particles' trajectories to calculate and deposit the spectral properties of the emitted radiation in a virtual detector, similar to the one depicted in Figure 2.1.

One of the most relevant results provided by JRad is possibly the simulation of X-ray emission from a plasma based particle accelerator, useful for modeling and developing a next-generation x-ray source. These sources are capable of producing synchrotron-like radiation in a tabletop device [19].

While physical processes like radiation emission can be fully described from the phase space trajectory of the system, in general, this is not the best approach, as it requires storing a large amount of memory (~ 100 TB per run). In order to avoid this problem, some sort of pre-selection is usually performed (*e.g* considering only a subset of the particles), leading to a loss of information. Therefore, run-time tools that calculate the radiation as the simulation runs are, undoubtedly, more desirable.

Implementation of large scale Particle In Cell codes in GPU systems was made possible with the recent improvements in GPU parallel computing. PIConGPU was the first scalable GPU cluster im-

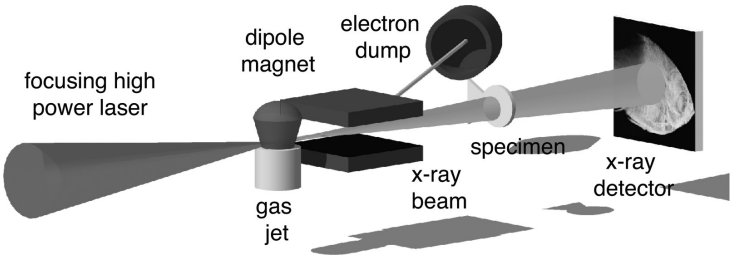

Figure 1.6: Sketch of the experimental setup designed with insight form JRad simulations. A high power laser hits a gas jet, creating a plasma wave, accelerating the electrons. The resulting x-rays can be used among other things to image bio-medical specimens. Adapted from Kneip et al. [20]

plementation of the fully relativistic PIC algorithm in plasma physics [21]. It was developed in 2010, at the Radiation Institute of the Helmholtz-Zentrum Dresden-Rossendorf laboratory, and is a promising alternative to the conventional CPU based Particle In Cell codes, like OSIRIS.

Efforts have also been made to incorporate a radiation diagnostic on PIConGPU. The massively parallel features of this PIC code make it easier to efficiently compute the spectral characteristics of radiation in run-time. As suggested by Pausch et al. [18], the radiation spectrum may be obtained through a summation of the integrand of Equation (1.3) over the simulation time steps:

$$\frac{d^2I}{d\omega d\Omega} \sim \left| q \sum_{t=t_{start}}^{t_{end}} \frac{\mathbf{n} \times [(\mathbf{n} - \boldsymbol{\beta}) \times \dot{\boldsymbol{\beta}})]}{(1 - \boldsymbol{\beta} \cdot \mathbf{n})^2} e^{i\omega(t_{\text{ret}} + R(t_{\text{ret}})/c)} dt_{\text{ret}} \right| . \tag{1.5}$$

The expression inside the summation of Equation (1.5) can be easily updated and added to the previous values in each iteration so that at the end of the simulation we are left with the full summation. This method makes it possible to calculate the radiation in run-time without storing the particles' trajectories.

This algorithm has been successfully benchmarked with known results for particle radiation. Figure 1.7 displays the comparison between the theoretical predictions and the results of the simulation for the nonlinear Thomson scattering of an electron bunch [22].

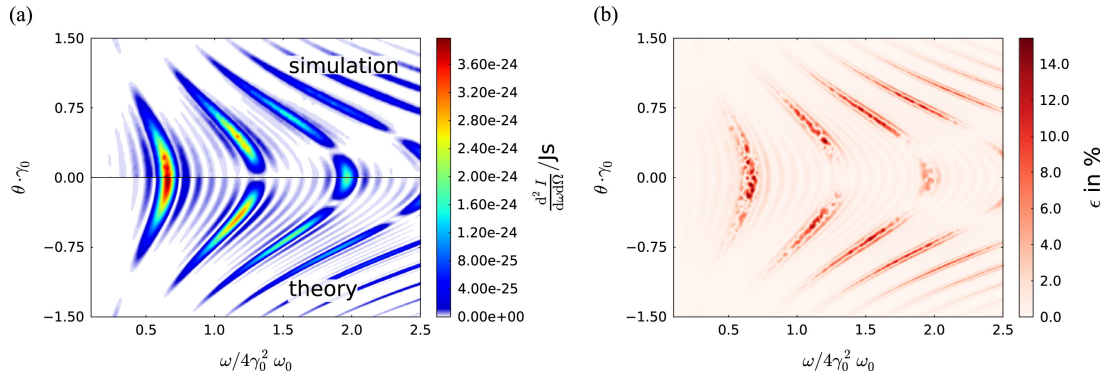

Figure 1.7: Both spectra are symmetrical with respect to $\theta\gamma_0$. a) represents the top half of the simulated spectrum and the bottom half of the theoretical predictions which are supposed to mirror each other. b) displays the relative difference between simulation and theory, the maximum error is $< 15\%$. Taken from Pausch et al. [18]

The most relevant advantage of the PIConGPU radiation diagnostic is the fact that it is a run-time tool which is not limited by the amount of memory available for storing particle's trajectories. Instead, it is mainly limited by computational costs associated to calculating the quantities defined on Equation (1.5). However, like JRad, this is a spectral diagnostic which is mainly focused on the spectral properties of ra-

diation, making it more difficult to access the spatiotemporal features of radiation and leaving properties like the OAM unexplored. With this work, we aim to study these unexplored features using a run-time diagnostic in OSIRIS and a post-processing tool.

1.5 Objectives

After the success of the diagnostic for radiation, JRad, several attempts were made to develop a post-processing tool that could describe the spatiotemporal properties of plasma radiation. First, A. Sainte-Marie [23], also working with GoLP, and then A. Reboul-Salze [24] developed such tools and successfully benchmarked their codes with some well known scenarios, however, the efficiency obtained for the calculations performed was not satisfactory.

These attempts showed that the spatiotemporal features of the radiation could be retrieved, being a critical first step in the development of a production tool. This thesis describes the implementation of such a tool, as a massively parallel tool, able to take full advantage from supercomputers, and a restructuration of the algorithm itself to make it compatible with OSIRIS, such that radiation can be obtained at run-time during the OSIRIS simulations potentially, opening the way to retrieve the contribution from every simulation particle.

Our goal is then to implement the radiation algorithm both inside OSIRIS and as a post-processing tool, and after benchmarking with well known examples, use it to discover the unknown spatiotemporal features of radiation in relevant scenarios.

1.6 Thesis Outline

The work developed on this thesis follows the processes of implementation, benchmarking and testing of a radiation code capable of detecting the spatiotemporal features of plasma generated light.

The implementation stage is described in Chapter 2, where the code's features are explained in detail. In this chapter we go through key aspects, such as the relevant approximations, the parallelization strategy, and the interpolation scheme.

In Chapter 3, we obtain theoretical expressions for some well known scenarios and compare these results with the ones obtained with the radiation diagnostic. The code is further benchmarked against the post-processing spectral code JRad. Additionally, the results of both the post-processing and run-time version of the radiation diagnostic are benchmarked against one another. Finally, the code's performance and parallel scalability are tested in some of the world's most powerful supercomputers.

Chapter 4 contains the results of applying the developed diagnostic in Plasma Wakefield Acceleration scenarios, where the previously undiscovered spatiotemporal properties of betatron radiation are thoroughly analyzed.

Finally, in Chapter 5, with the aim of bringing the simulation's results closer to real laboratory results, we discuss the effect of the macroparticles in the simulation on the radiation profile.

Chapter 2

Implementation Details

A radiation calculation algorithm was implemented in OSIRIS, as a run time diagnostic, taking advantage of its parallel features and object-oriented organization. Moreover, this diagnostic was complemented with a post-processing tool that recovers the spatiotemporal signature of the radiation from the trajectories generated by OSIRIS. Both tools were implemented in Fortran 2003. In this section we discuss the approach taken in order to incorporate the radiation algorithm in this framework.

2.1 Numerical model

As seen in the previous chapter, the radiation emitted by a particle can be obtained through the acceleration fields if the detector is far enough. In this way, the electromagnetic radiation for each position and time at the detector can computed using the following expression, where all quantities are defined as in the previous chapter:

$$\mathbf{E}(\mathbf{x}, t = t_{\text{det}}) = \frac{e}{c}\left[\frac{\mathbf{n}\times[(\mathbf{n}-\boldsymbol{\beta})\times\dot{\boldsymbol{\beta}})]}{(1-\boldsymbol{\beta}\cdot\mathbf{n})^3 R}\right]_{\text{ret}}, \qquad \mathbf{B}(\mathbf{x}, t) = [\mathbf{n}\times\mathbf{E}]_{\text{ret}}\,. \tag{2.1}$$

However, the radiated fields only arrive at the detector after a certain time period, as shown in Figure 2.1. In fact, the above equation suggests that for each detector's time slot, t_{det}, the fields should be calculated by finding the corresponding retarded time of the particle's trajectory, t_{ret} and then use the position and momenta at that time. However, this is not feasible in a run-time scenario as it would require full knowledge about every trajectory, which is only available after the simulation is run.

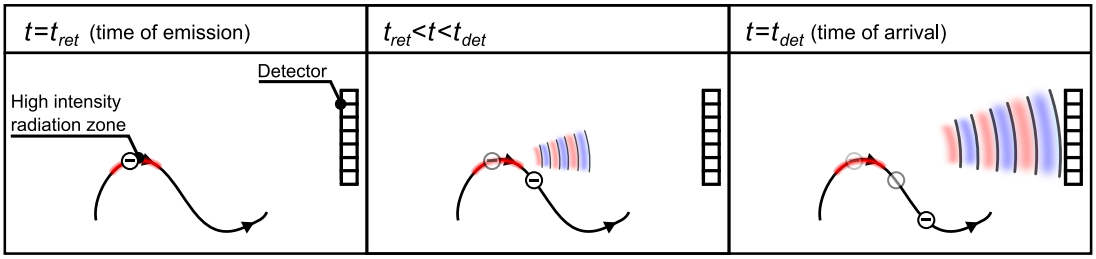

Figure 2.1: Sketch of the emission of radiation by a charged particle. Radiation is mostly emitted along the direction of particle's velocity. This radiation only arrives to the detector after some Δt.

The correct strategy is therefore to do the inverse operation: Take each time-step of the simulation (t_{sim}) as a retarded time ($t_{\text{ret}} = t_{\text{sim}}$), and compute the time at which the radiation arrives at the detector ($t_{\text{det}} = R_{t=t_{\text{ret}}}/c + t_{\text{ret}}$) and then use the available simulation quantities to compute and deposit the electromagnetic field:

$$\mathbf{E}(\mathbf{x}, t = t_{\text{det}}) = \frac{e}{c}\left[\frac{\mathbf{n} \times [(\mathbf{n} - \boldsymbol{\beta}) \times \dot{\boldsymbol{\beta}})]}{(1 - \boldsymbol{\beta} \cdot \mathbf{n})^3 R}\right]_{t=t_{\text{sim}}}, \qquad \mathbf{B}(\mathbf{x}, t = t_{\text{det}}) = [\mathbf{n} \times \mathbf{E}]_{t=t_{\text{ret}}=t_{\text{sim}}}\,. \tag{2.2}$$

This strategy, which can be implemented in both the run-time and post processing version, is summarized in Algorithm 1. It comprises two different loops: one through all the radiative particles and another through the detector's cells, both potentially parallelizable.

Algorithm 1 Radiation calculation and deposition

procedure RADIATIONCALCULATOR ▷ To be used inside the PIC loop, after pushing particles
  for all $particle$ **in** simulation **do**
    for all $cell$ **in** detector **do** ▷ The inner and outer loops are potentially parallelizable
      $\mathbf{n} \leftarrow$ direction$(particle, cell)$
      $\beta \leftarrow$ velocity$(particle)$
      $\dot{\beta} \leftarrow$ acceleration$(particle)$
      $R \leftarrow$ distance$(particle, cell)$
      $t_{\text{det}} \leftarrow R/c + t$
      if $t_{\text{det}}min < t_{\text{det}} < t_{\text{det}}max$ **then**
        $\boldsymbol{E}(cell, t_{arrive}) \leftarrow \mathbf{E}(\mathbf{n}, \beta, \dot{\beta})$ ▷ Obtain the Liénard-Wiechert field using equation (2.1)

With this approach, the algorithm only needs to loop through the spatial cells of detector as the time of deposition is calculated for each spatial cell. This means that the temporal resolution can be increased without affecting the computational load. However, it is important to note that a larger resolution can also imply a larger detector which eventually leads to longer communications.

2.1.1 Far Field approximation

Computing the time of arrival of the radiation at a given cell in the detector usually requires three different operations:

i) Finding the vector that points from the particle to the detector's cell $\mathbf{r} = \mathbf{r}_{part} - \mathbf{r}_{cell}$,

ii) Computing its norm, $R = ||\mathbf{r}||$,

iii) Adding this value to the time of emission $t_{\text{det}} = R/c + t_{\text{ret}}$.

Although these three operations may seem quite harmless to the code's performance, when the computational load increases, either due the a large number of particles in the simulation or large number of cells in the detector, their contribution to the overall run time increases and may dominate over the total simulation time. With this in mind, an optional feature was added to the algorithm: the so-called far-field approximation.

This approximation is especially useful for a spherical detector, but the same principle can be applied to other geometries. In a spherical surface (or a segment of it) centered at the origin (0,0,0), every cell is

at the same distance, R_{cell}, from the origin. If this distance is sufficiently higher than the distance from the particle to the origin, the calculation of the distance R and the time of arrival $t_{arrive} = t_{\text{det}}$ can be simplified using the fact that $\sqrt{1+x} \simeq 1 + x/2$ for $x \ll 1$.

$$\begin{aligned} R =& ||\mathbf{r}_{cell} - \mathbf{r}_{part}|| = \sqrt{(\mathbf{r}_{cell} - \mathbf{r}_{part}) \cdot (\mathbf{r}_{cell} - \mathbf{r}_{part})} \\ =& \sqrt{||\mathbf{r}_{cell}||^2 + ||\mathbf{r}_{part}||^2 - 2\mathbf{r}_{cell} \cdot \mathbf{r}_{part}} \\ =& ||\mathbf{r}_{cell}|| \sqrt{1 + \frac{||\mathbf{r}_{part}||^2}{||\mathbf{r}_{cell}||^2} - 2\frac{\mathbf{n}_{cell} \cdot \mathbf{r}_{part}}{||\mathbf{r}_{cell}||}} \\ \simeq& R_{cell} - \mathbf{r}_{part} \cdot \mathbf{n}_{cell} \quad , \quad t_{det} = t_{ret} + R_{cell} - \mathbf{r}_{part} \cdot \mathbf{n}_{cell} \end{aligned} \tag{2.3}$$

The time of arrival can then be remapped to $\tilde{t}_{det} = t_{det} - R_{cell} = t_{ret} - \mathbf{r}_{part} \cdot \mathbf{n}_{cell}$ in order to avoid scaling issues that arise due to the orders of magnitude that usually separate the detector's radius and the variations in $\mathbf{r}_{part} \cdot \mathbf{n}_{cell}$ ($\sim 10^5$).

2.2 Implementation of an Object-oriented environment

In OSIRIS, the information about the simulation's particles is stored in objects of the class *species* (Figure 2.2a), which contain information about the particles' instantaneous state. However, as shall become apparent in the following sections, the radiation algorithm requires information about the *previous* state of the particles.

For example, as suggested by Equation (2.2), computing the emitted radiation requires information about the acceleration of the particle, which can only be obtained using the velocity of the particle at the previous time step. In order to cope with this requirement, Fortran 03 enables the creation of an extension of the *species* class, whose objects contain all attributes and procedures of the original class as well as additional members that may be defined. In this way, a new class called *species_radiat* (Figure 2.2b) was created in OSIRIS. Its objects contain data on the previous position and momentum as well as the methods to calculate and deposit electromagnetic radiation in the detector object. This object-oriented philosophy was also used in the post-processing code, where the detector was also idealized as an object with its own deposition methods and data structures.

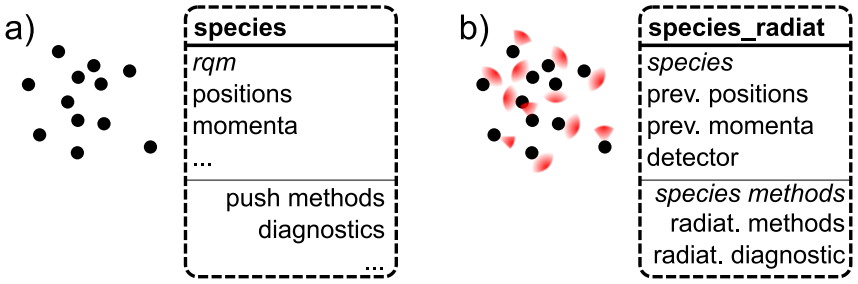

Figure 2.2: Illustration of the main differences between the *species* and *species_radiat* objects. The radiative species contains all the atributes and methods of the standard species object.

2.3 Detector

A key feature of the radiation diagnostic is the virtual detector. It is the region of space where radiation is tracked during a given time period. This time period is usually different from the simulation time, as the detector often needs to have a higher time resolution than the PIC simulation. This way, it can be defined as a 4-D grid with any given shape. Two types of detectors were implemented (Figure 2.3): a spherical one, where the grid is defined using spherical coordinates $(\mathbf{e}_\theta, \mathbf{e}_\phi, \mathbf{e}_\mathbf{r})$ and a cartesian one, where the grid is defined using cartesian coordinates $(\mathbf{e}_\mathbf{x}, \mathbf{e}_\mathbf{y}, \mathbf{e}_\mathbf{z})$.

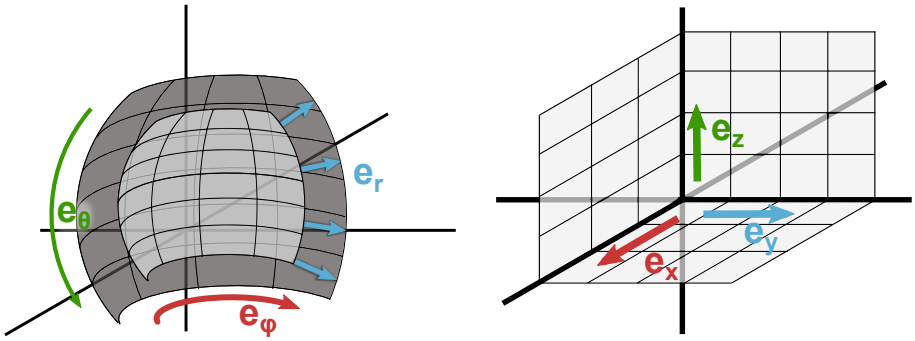

Figure 2.3: Spherical (left) and cartesian (right) detectors. The darker spherical grid has a higher radius than the lighter one. All spherical grids are centered in the origin of the coordinate system.

In each step of the simulation (or the trajectory, in the post-processing code), the radiation algorithm loops through the spatial cells of the detector, finding the correct time cell for depositing the calculated radiation. However, it is highly unlikely that the deposition time matches the discretized time grid of the detector. Therefore, in order to figure out exactly how much radiation should be deposited in each time slot, an interpolation is required.

2.4 Deposition of the radiated fields in the virtual detector

In OSIRIS, the calculation and deposition of the emitted radiation take place in a sub-step of the PIC loop created specifically for that purpose. As shown in Figure 2.4, this sub-step comes right after pushing the particles, in such a way that the newly calculated positions and velocities can be used to compute the required quantities for the radiation calculation. In the post-processing version, each step of the trajectory corresponds to a full PIC loop, and the code computes the radiation at each trajectory step as it loops through the track.

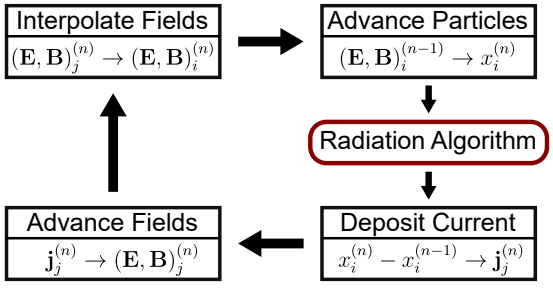

Figure 2.4: Modified PIC loop with the addition of the radiation calculation procedure.

In the likely event that the time of deposition does not match any of the discretized time steps of the detector, an interpolation must be performed in order to deposit the fields across different detector cells. The simplest method would be the so called *closest point approximation*, which consists in depositing the radiation fields at the closest time step. In spite of its simplicity, this strategy, which corresponds to an instantaneous detector, may lead to some problems, such as conflicting values for the same time step or double counting when the closest time step is the same for different depositions, as shown in Figure 2.5(a) where the depositions of the radiation emitted at the retarded times t_2' and t_3' happen at the same time slot.

These issues can be avoided with an integrator detector, which weighs the contribution of each deposition by the time until the next deposition. Therefore, the value of the radiation in a time slot is the integral of the radiation in the interval delimited by two consecutive time-steps. This corresponds to what a real detector would capture Figure 2.5(b) shows an example case that clarifies this deposition scheme. In this example, t_i refers to the detector's time grid and t_i' to the different deposition times. Each of these depositions corresponds to radiation emitted at different simulation time steps, in this context, this interpolation can be performed while the simulation is running as it only requires information about the radiated field in the previous time step. The example present in Figure 2.5(b) the deposition algorithm would go as follows:

- **Iteration 1**: The radiation arrives at the detector at $t = t_2'$.

  $E(t_1')(t_2 - t_1')/dt$ is deposited in the first time slot, t_1.

  $E(t_1')(t_2' - t_2)/dt$ is deposited in the second time slot, t_2.

- **Iteration 2**: The radiation arrives at the detector at $t = t_3'$.

  $E(t_2')(t_3' - t_2')/dt$ is deposited in the second time slot, t_2.

- **Iteration 3**: The radiation arrives at the detector at $t = t_4'$.

  $E(t_3')(t_3 - t_3')/dt$ is deposited in the second time slot, t_2.

  $E(t_3')(t_4 - t_3)/dt$ is deposited in the third time slot, t_3.

  $E(t_3')(t_4' - t_4)/dt$ is deposited in the fourth time slot, t_4.

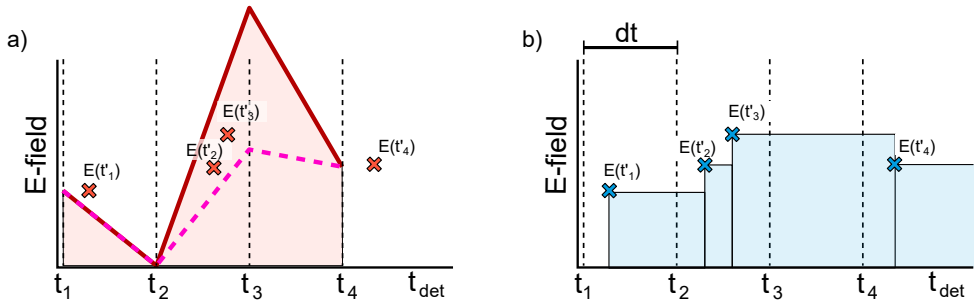

Figure 2.5: Different possible deposition schemes. a) Instantaneous detector: radiation is deposited in the time slot closest to t_{dep}. When two consecutive deposition happen in the same time slot the fied value becomes undefined, as it could either be double counted (solid red line), overwritten or averaged (pink dashed line). b) Integrator detector: radiation is deposited in the time slot in which it arrived after being scaled by the time until the next deposition

Using this approach, radiation can be computed and deposited using only the information from the current and the previous time steps. The fields are always calculated at the previous time step using the previous position and momentum and the integration is accomplished using the previous deposition time. This ensures that $\int \mathbf{E} dt$ does not vary if detectors with different resolution are employed. the field values in the detector thus correspond to the integrated fields emitted over a detector cell which ensures a smoother field profiles in comparison to an instantaneous deposition scheme, as evidenced by Figure 2.5.

2.5 Parallelization

The radiation algorithm consists in two loops, one that circles through the N_p particles and another one that, for each particle, circles through the N_c detector cells, performing $\sim N_p N_c$ operations. While the particle loop can only be parallelized using distributed memory parallelization due to concurrence problems that arise when two or more particles deposit radiation in the same detector object, the detector loop can be parallelized using shared memory parallelization.

The parallelization scheme in OSIRIS is illustrated in Figure 2.6(a). It consists in dividing the simulation domain in segments, assigning each segment to a single processor, in such a way that each processor only deals with a specific region of space. Information about the particles that cross regions and the fields or currents at the boundaries are shared between processors using the Message Passing Interface (MPI). This parallelization strategy was proposed by Wang et al. [25] and has been proven to be very effective ($> 95\%$ efficiency) and highly scalable for systems with many particles. A mixture of shared and distributed memory parallelization using OpenMP together with MPI is also supported, but in general, only MPI is used.

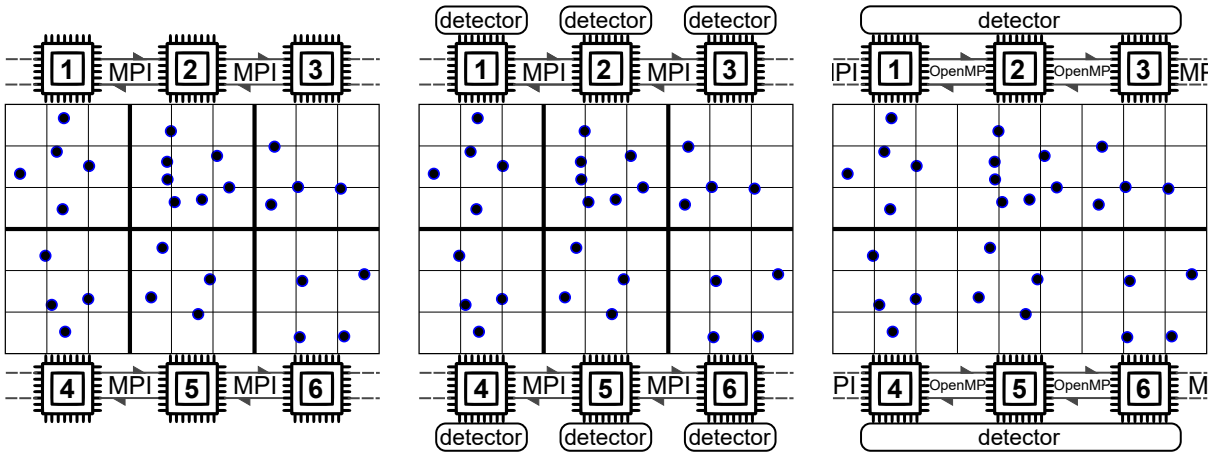

(a) OSIRIS distributed memory parallelization scheme

(b) RaDiO distributed memory parallelization with domain decomposition

(c) RaDiO hybrid distributed-shared memory parallelization

Figure 2.6: Comparison between the standard OSIRIS parallelization and the parallelization of the radiation diagnostic. Each of the represented CPU's may have multiple cores that can be used to further parallelize operation in each sub-region using OpenMP. This cluster architecture is fairly common in current supercomputers.

This diagnostic uses a parallelization scheme that makes use of this decomposition by assigning a copy of the detector to each sub-domain, as depicted in Figure 2.6(b). Thus, each Distributed Memory Processor (DMP) deals with radiation emitted by the sub-group of particles that belong to its region.

In the post-processing code, the parallelization is also accomplished by creating sub-groups of particles. However, each sub-group is not bound to a specific region of the simulation. Whenever the code reports the detector, each copy is summed into a single detector using MPI before writing the data to the disk. This method almost fully avoids communications between processors during the rest of the simulation and therefore does not affect the overall parallel efficiency.

Distributed-shared memory hybrid parallelization was also implemented, but kept as an optional feature. This scheme is similar to the one described in the previous paragraph, the only difference being that instead of assigning a single DMP to a sub-group of particles, several Shared Memory Processor (SMP) are used to calculate the radiation of the particles present in a sub-group using a single detector which is split among the SMPs, as shown in Figure 2.6(c). In this way, if the total number of processors is kept constant , the number of region sub-domains decreases, which leads to a decrease in the amount of memory and communications required when compared to the previous scheme. In theory, this does not lead to a loss of parallel efficiency as in both cases each processor deals with the same amount of radiation calculation operations, however this is only true for radiation calculations as not all steps in the PIC loop can be parallelized by shared memory, often resulting in an increase of operations per processor.

While the use of OpenMP for parallelism may not scale perfectly within the context of OSIRIS simulations, as the shared memory parallelization of the PIC algorithm requires additional operations to be performed, the same issue does not emerge in the post-processing case, as all its operations potentially benefit from shared memory parallelization.

2.6 Documentation of the algorithm

An extensive guide to the code's compilation and usage as well as some theoretical background and some general guidelines on how to obtain significant results can be found on a wiki created specifically for this purpose and will be publicly available to OSIRIS users as soon as the code is officially included into the latest OSIRIS release. RaDiOWiki, the wiki page for the Radiation Diagnostic for OSIRIS is currently still in development, but contains all the necessary information for operating the code. Some examples of what can be found in that page are shown in Figure 2.7.

The simulation parameters are usually specified in external files called input-decks. In OSIRIS, these files contain information about the simulation domain, its number of species or type of pusher to be used, among others. With the addition of the radiative species, came the need to specify the detector parameters to be used. So, in this new version of OSIRIS, the users may specify any number of detectors for a single radiative species by adding sections called either *spherical* or *cartesian* before the *species* section in the input-deck. In these sections of the input-deck, the users specify key properties of the detector, such as is timespan and spatial region or the components of the EM fields it detects.

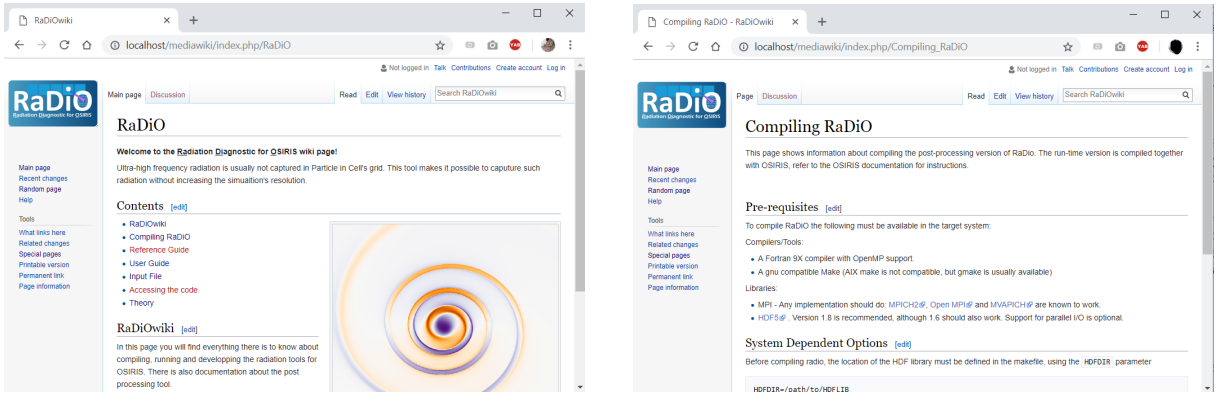

Figure 2.7: Snapshots of RaDiOWiki.

The post-processing code also accepts input-decks that specify the properties of the detector. Some examples of these input-decks, can also be found in Appendix A.

Chapter 3

Benchmarks and performance

The spatiotemporal behaviour of the radiation emitted by charged particles either in a plasma or a synchrotron environment remains fairly unexplored and to the best of our knowledge, no theoretical predictions have been made on the spatiotemporal signature of any kind of motion. However, the spectral properties of radiation are well documented for some common types of motion as typical synchrotron light sources generate radiation by making relativistic, ultra-fast particles undergo a sinusoidal or helical motion inside periodic magnetic structures known as *wigglers* or *undulators*. Such conditions can also be obtained in a plasma using relativistic plasma waves [14] instead of magnetic structures or EM fields. These spectra can be obtained by performing a Fast Fourier Transform (FFT) on the spatiotemporal detector, making it possible to benchmark the results against the theoretical predictions for the radiated spectrum.

In this way, several radiation favorable scenarios have been idealized and thoroughly studied to the point where accurate theoretical predictions can be made. The conditions required for these predictions to hold are usually not met in collective systems of particles, where coherence effect may be present, as the interactions between particles normally affect their trajectories, introducing deviations from the ideal sinusoid or helix. As a result, these tests were performed either with artificially-generated single-particle trajectories via the post-processing radiation diagnostic or with single-particle PIC simulations. Furthermore, the run-time radiation diagnostic was benchmarked against the post processing code by comparing the radiation obtained directly from an OSIRIS run with the radiation obtained from the trajectories originated by the same run. Simulations in this chapter often use a single particle, in that case, the normalizations of Table 1.1 no longer make sense as there is no plasma involved. Therefore, in this chapter, ω_p and n_0 are just arbitrary normalization constants.

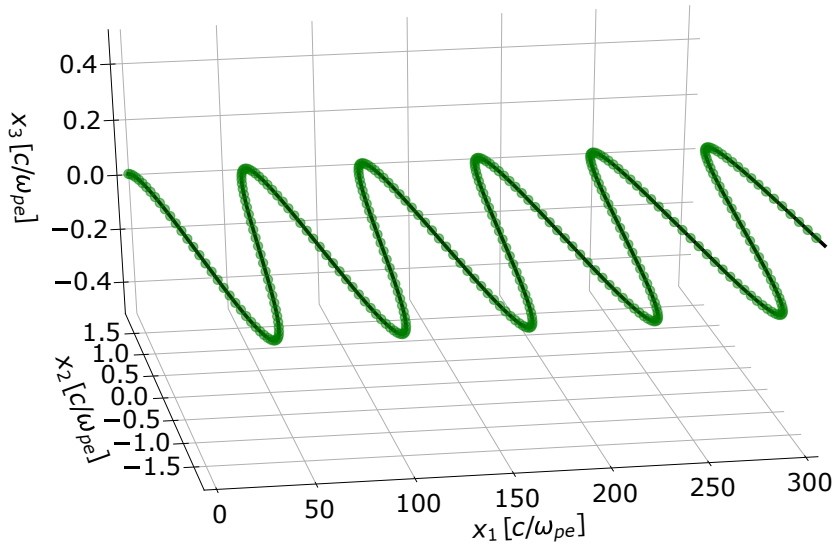

Figure 3.1: Sinusoidal trajectory of a charged particle. Relativistic particle undergoing a sinusoidal motion on the x_2 axis while moving forward in the x_1 direction. $\gamma = 50$.

3.1 Sinusoidal trajectories in a plane

This is one of the most common types of trajectories imposed by wiggler and undulator mechanisms. According to the previous section, a charged particle undergoing a sinusoidal trajectory like the one depicted in Figure 3.1 will radiate with maximum intensity at the peaks of the trajectory and in the direction of the particle's longitudinal velocity.

The shape of the emitted radiation spectrum depends on the properties of the sinusoidal trajectory. In particular, it depends on the K parameter, often called the wiggler strength parameter, which can be thought of as a scaled angle because it is defined as the product of the Lorentz factor, γ, and the maximum angle of the particle's trajectory, ψ_b. Therefore, $K = \gamma\psi_b = \gamma r_b k_b$, where r_b and k_b are, respectively, the amplitude and spatial frequency of the trajectory, which is given by $x_2(x_1) = r_b \sin(k_b x_1)$ and $x_1(t) = \beta t$. The K parameter determines the number of harmonics present in the spectrum [15]: for $K \ll 1$, at the so-called *undulator* regime, there is only one significant harmonic in the spectrum whereas for $K \gg 1$, at the so-called *wiggler* regime, higher harmonics are generated, resulting in a broader spectrum. In his work about synchrotron radiation in plasma focusing channels, Esarey et al. [9] established that the peak intensity of the harmonics present in the radiated spectrum on axis (*i.e.* $x_2 = 0$ on Figure 3.1) is merely dependent on an amplitude function F_n:

$$F_n = n\alpha_n \left[J_{(n-1)/2}(\alpha_n) - J_{(n+1)/2}(\alpha_n)\right]^2, \quad \text{with } \alpha_n = \frac{nK^2/4}{1 + K^2/2} \tag{3.1}$$

where n is the order of the harmonic and $J_n(x)$ the Bessel Functions of the first kind. Figure 3.2 shows the behaviour of the harmonic peak intensity for the first 5 odd harmonics. It evidences that number of relevant harmonics increases as K rises above the unity. When K tends to 0, only the fundamental harmonic ($n = 1$) survives, as all the other harmonics vanish before that point. However, as K approaches 1, the higher harmonics start to become more intense, which means that the spectrum will be composed of a larger number of harmonics.

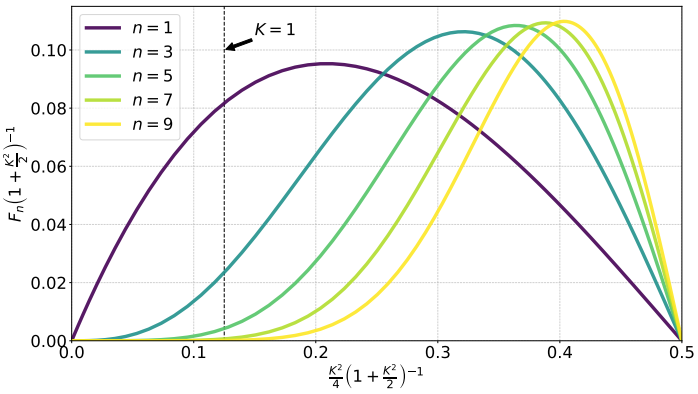

Figure 3.2: Amplitude functions for the first 5 odd harmonics as a function of $\frac{K^2}{4}\left(1+\frac{K^2}{2}\right)^{-1}$. The vertical line marks the $K=1$ boundary.

The wiggler regime can be attained with a highly relativistic particle (*i.e.* $\gamma \gg 1$). In these conditions, the higher intensity radiation, which is the one emitted at the peaks of the trajectory, can be approximated by the radiation of a particle undergoing a locally circular trajectory [15] with radius ρ and linear velocity v as depicted in Figure 3.3. As a result, the expected radiation spectrum for such trajectory can be found using the following equation :

$$\frac{d^2I}{d\omega d\Omega} = \frac{q_e^2\omega^2}{4\pi^2 c}\left|\int_{-\infty}^{\infty} \mathbf{n}\times(\mathbf{n}\times\boldsymbol{\beta})e^{i\omega(t_{\text{ret}}-\frac{\mathbf{n}\cdot\mathbf{r}}{c})}dt_{\text{ret}}\right|^2 \tag{3.2}$$

The velocity of the particle is given by $\boldsymbol{\beta} = \beta\left[\sin(vt/\rho)\mathbf{e_{x_1}} + \cos(vt/\rho)\mathbf{e_{x_2}}\right]$ and the position, $\mathbf{r}$, by $\mathbf{r} = \rho\sin(vt/\rho)\mathbf{e_{x_1}} + (1-\rho)\cos(vt/\rho)\mathbf{e_{x_2}}$. Moreover, the direction vector $\mathbf{n}$ is chosen to lie on the plane perpendicular to the trajectory, in such a way that the relevant parts of equation, the vector part and the exponential argument in Equation (3.2) can be computed for small enough variations in θ and vt/ρ, as well as $\beta \simeq 1$:

$$\mathbf{n}\times\mathbf{n}\times\boldsymbol{\beta} = \theta\mathbf{n}\times\mathbf{e_{x_2}} - \left(\frac{ct}{\rho}\right)\mathbf{e_{x_2}}, \quad \omega\left(t-\frac{\mathbf{n}\cdot\mathbf{r}}{c}\right) = \omega\left[\left(\frac{1}{\gamma^2}-\theta^2\right)t - \frac{c^2}{3\rho^2}t^3\right]. \tag{3.3}$$

The integral on Equation (3.2) can thus the be written as:

$$\frac{d^2I}{d\omega d\Omega} = \frac{q_e^2\omega^2}{4\pi^2 c}\left|\int_{-\infty}^{\infty} \exp\left(i\omega\left[\left(\frac{1}{\gamma^2}-\theta^2\right)t - \frac{c^2}{3\rho^2}t^3\right]\right)\left[\theta\mathbf{n}\times\mathbf{e_{x_2}} - \left(\frac{ct}{\rho}\right)\mathbf{e_{x_2}}\right]dt\right|^2. \tag{3.4}$$

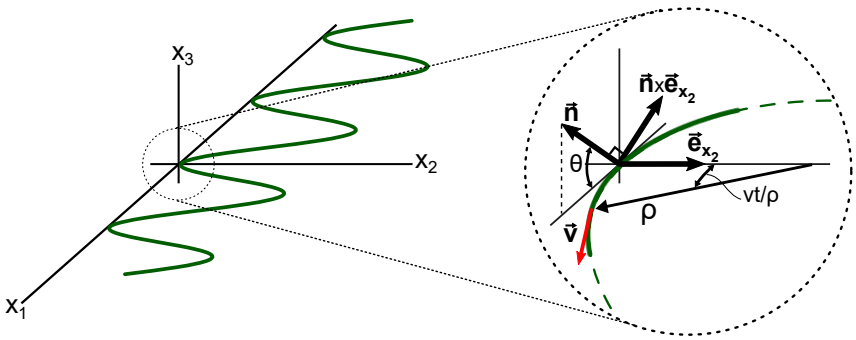

Figure 3.3: Circular motion approximation of a sinusoidal trajectory. The particle is assumed to move along a circumference of radius ρ with linear velocity v and angular velocity v/ρ.

with the proper variable substitutions $x = ct/\rho\left(\gamma^{-2}+\theta^2\right)^{-1/2}$, and $\Upsilon = \frac{\omega\rho}{3c}\left(\gamma^{-2}+\theta^2\right)^{-3/2}$ and taking into account the parity of both components of the integrand, a simpler version, recognizable as modified Bessel functions K_n can be obtained:

$$\begin{aligned}\frac{d^2I}{d\omega d\Omega} &= \frac{q_e^2\omega^2\rho^2}{4\pi^2c^3}\left(\frac{1}{\gamma^2}+\theta^2\right)^2\left|\int_{-\infty}^{\infty}\frac{\theta}{\sqrt{\gamma^{-2}+\theta^2}}\cos\left[i\frac{3}{2}\Upsilon\left(x+\frac{x^3}{3}\right)\right]\mathbf{n}\times\mathbf{e_{x_2}} - x\sin\left[i\frac{3}{2}\Upsilon\left(x+\frac{x^3}{3}\right)\right]\mathbf{e_{x_2}}dx\right|^2 \\ &= \frac{q_e^2\omega^2\rho^2}{4\pi^2c^3}\left(\frac{1}{\gamma^2}+\theta^2\right)^2\left|\frac{\theta}{\sqrt{\gamma^{-2}+\theta^2}}\frac{2}{\sqrt{3}}K_{2/3}(\Upsilon)\mathbf{n}\times\mathbf{e_{x_2}} - \frac{2}{\sqrt{3}}K_{1/3}(\Upsilon)\mathbf{e_{x_2}}\right|^2 \\ &= \frac{q_e^2\omega^2\gamma^2}{3\pi^2c\omega_\beta K}\left(\frac{1}{\gamma^2}+\theta^2\right)^2\left[\frac{\theta^2}{\gamma^{-2}+\theta^2}K_{2/3}^2(\Upsilon)+K_{1/3}^2(\Upsilon)\right]. \end{aligned} \tag{3.5}$$

Furthermore, the integration over all angles provides the following expression for the frequency distribution of the radiated energy:

$$\frac{dI}{d\omega} = \sqrt{3}\frac{q_e^2\gamma\omega}{c\omega_c}\int_{\omega/\omega_c}^{\infty}K_{5/3}(x)dx \tag{3.6}$$

where ω_c is known as the critical frequency, given by $\omega_c = \frac{3}{2}\gamma^3\frac{c}{\rho}$, which can be defined as the frequency for which $\Upsilon = \frac{1}{2}$ for $\theta = 0$. The critical frequency can be written in terms of the trajectories frequency, ω_β using the fact that the radius , ρ, is given by $\rho = \frac{\gamma}{k_bK} = \frac{c\gamma}{\omega_\beta K}$. Hence, $\omega_c = \frac{3}{2}\gamma^2\omega_\beta$.

In order to benchmark the code's results, we generated a trajectory with $K = 10 \gg 1$, using an ultra-relativistic electron ($\gamma = 50$) with an amplitude $r_b = 2\,c/\omega_p$ and $k_0 = 0.1\,\omega_p/c$ (Figure 3.1). This trajectory was then analyzed with the post-processing code using a slice of a spherical detector, placed in the x_3x_1 plane, $10^5\,c/\omega_p$ away from the axis origin with an angular aperture of 0.1 rad around the x_1 axis.

The results from RaDiO are shown in Figure 3.4 which features a plot of the detected electric field in the $\mathbf{e}_\phi$ direction for each spatiotemporal cell. The radiation is composed of several periodically spaced peaks, whose temporal shape can be observed in the lineouts. Furthermore, it is possible to note that for higher angles these peaks arrive later and are broader, creating the paraboloid structures that can be seen in the upper plot. This dephasing becomes more significant as the particle approaches the detector's surface, resulting in a decrease of the parabolas' opening. This effect is caused by the variation in the distance between the particle and the detector's cells, roughly given by $d_{pc} \simeq \sqrt{\left(x_1 - R\sin\theta\right)^2 + R^2\cos^2\theta}$, which clearly grows with both θ and x_1 for θ between 0 and π rad.

The comparison with the theoretical predictions presented in Equation (3.5) was achieved by taking the sum of the FFT of $E(t)$ in each direction with respect to time for each angle. The results are displayed in Figure 3.5. As the spectrum is symmetric with respect to θ, the comparison can be easily made by representing the two complementary halves of both the theoretical and simulated spectrum.

Even though both spectra feature exactly the same shape, there are some major differences, as the theoretical prediction seems to be much smoother than the simulation results. This is evidenced by the lineout displayed in the bottom plot, where the theoretical prediction is shown to be a smooth curve that envelopes the simulation results. This happens because the Equation (3.5) is an asymptotic

expression which is strictly valid for a large number of periods and $K \to +\infty$, ultimately corresponding to a superposition of all the harmonics. When K is lower the spectrum comprises a smaller number of harmonics and their superposition is set of peaks and valleys instead of a smooth curve.

Similar results can be obtained when using numerical algorithms that capture the spectrum of radiation directly (*e.g.* JRad). However, JRad uses a Cartesian detector whereas we employed a spherical detector in the RaDiO simulations in order to compare directly with theory. Nevertheless, because the angular aperture is much smaller than π, the effects of the curvature of the detector are effectively negligible, as shown in Figure 3.6, which features the full spectrum obtained with a cartesian detector. The shape of the spectrum matches both the theoretical envelope and the results from RaDiO.

Moreover, the integration of the spectrum over all angles yields the frequency distribution of the emitted radiation which can be benchmarked against Equation (3.6). In order to make this comparison, we ran a peak detection algorithm and measured the relative error between theory and simulation, as shown in Figure 3.7.

As before, the theoretical prediction is an envelope of the simulation results. Despite this fact, the comparison is excellent, as the intensity of most peaks matches the expected result with small relative error which rises as frequency increases. This happens not due an increase of absolute error, but by a decrease in the spectrum's value.

Since there is no trivial expression for the frequency integrated spectrum, $dI/d\Omega$, the best way to benchmark this spectrum is to do it against the result of the post-processing spectral code JRad. The outcome can be observed in Figure 3.8. This figure shows an almost perfect agreement between the results of both codes, which sit on top of each other with small error.

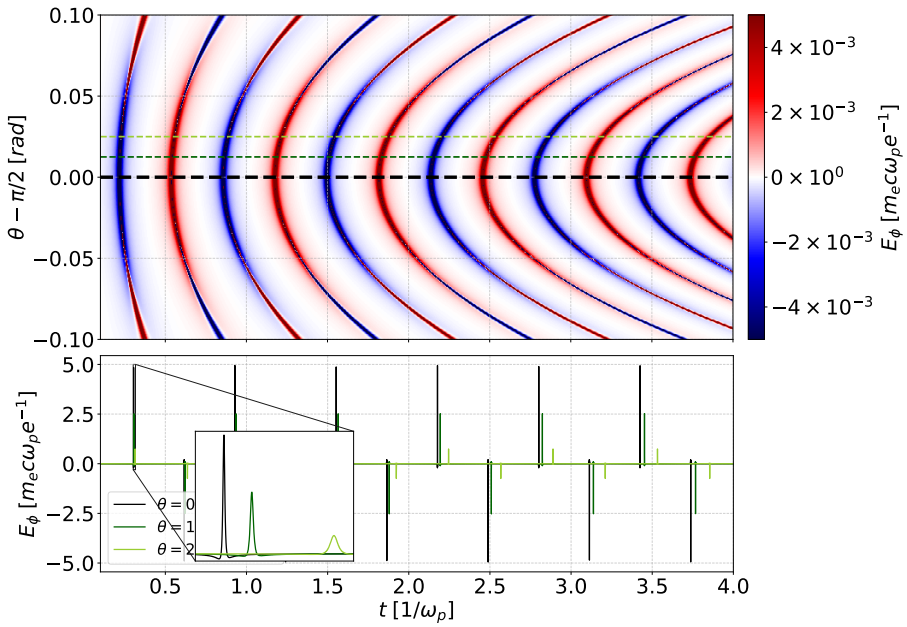

Figure 3.4: Spatiotemporal signature of the radiation emitted by a particle undergoing a sinusoidal motion in a transverse detector. The lineouts are shown on the bottom plot. This detector has 512 spatial cells and 131072 temporal cells, resulting in a temporal resolution of $2.98 \times 10^{-5} c/\omega_p$

.

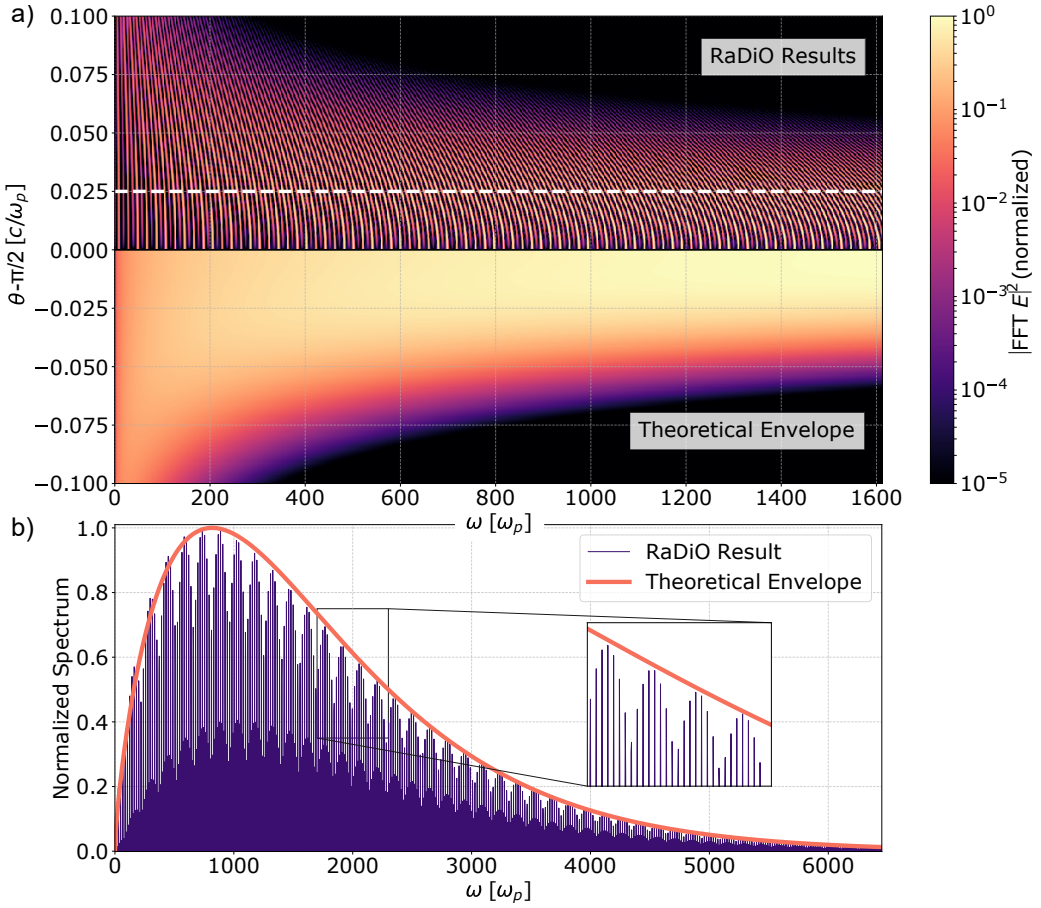

Figure 3.5: a) Comparison between the theoretical expectations for the radiated spectrum and the Post-processing code results for the radiated spectrum. b) Comparison between a lineout at $\Delta\theta = 0.02$ from both spectra.

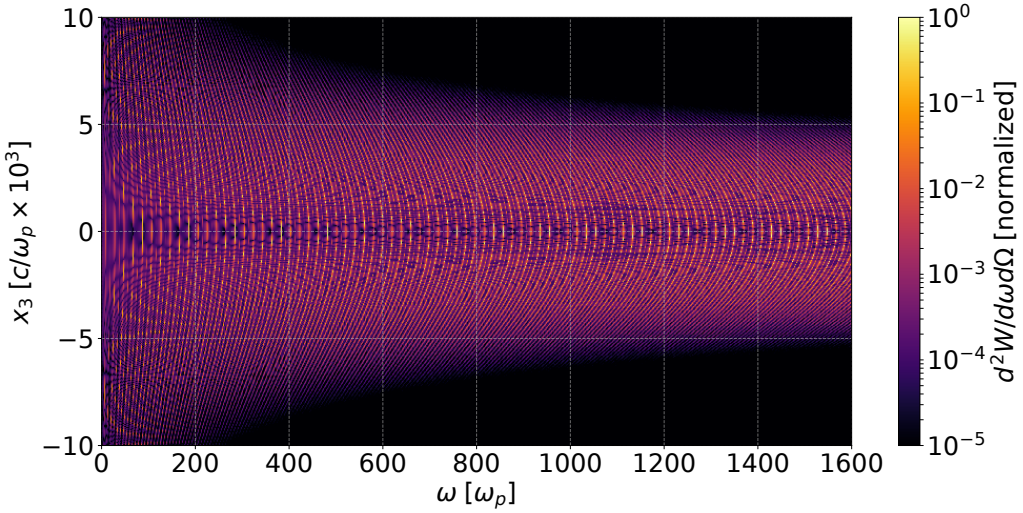

Figure 3.6: Radiation spectrum obtained with JRad. The cartesian detector has the same aperture as the spherical one used with RaDiO. This detector has 460 spatial cells and 32680 frequency cells.

3.2 Helical trajectories

Another common trajectory imposed by radiation generation setups is a helical trajectory, which can be seen as a composition of two sinusoidal trajectories in perpendicular planes. This trajectory, as depicted in Figure 3.9, was first proposed by Brian Kincaid [26] as an alternative to the conventional sinusoid

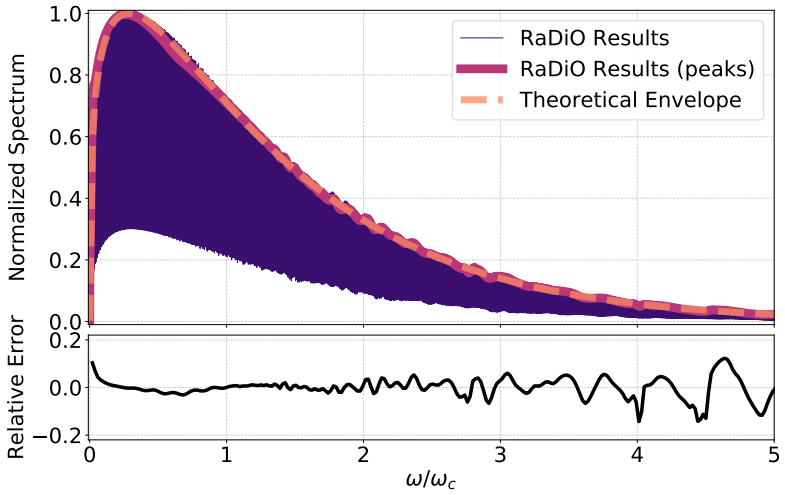

Figure 3.7: Angle integrated spectrum comparison, both spectra are normalized to 1 in order to make the comparison possible. The relative error is shown on the bottom plot.

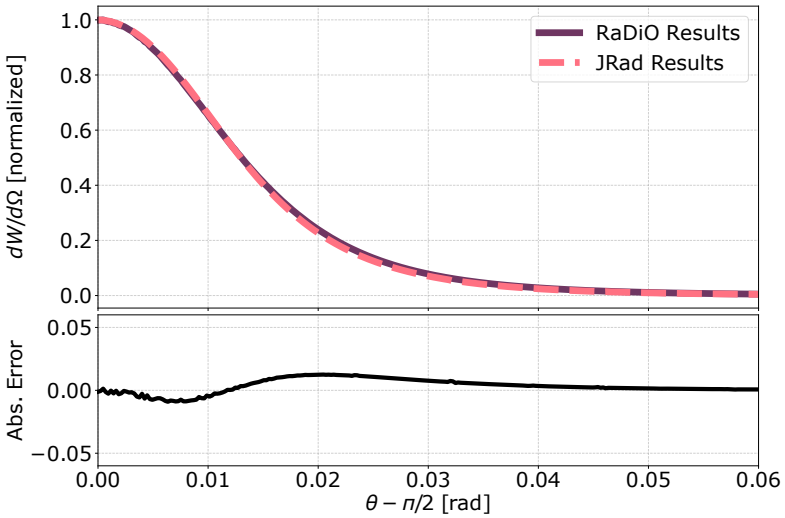

Figure 3.8: Frequency integrated spectrum comparison, both spectra are normalized to 1 in order to make the comparison possible. The relative error is shown on the bottom plot.

explored in the previous section, potentially yielding an improvement of several orders of magnitude in intensity and brightness.

In such conditions, the expected spectrum can be obtained using the same method as before, yielding the following result [26]:

$$\frac{d^2I}{d\omega d\Omega} = \frac{q_e^2\omega^2K^2}{\pi^2 c\omega_0^2\gamma^2}\sum_{n=1}^{+\infty}\left[J_n'^2(x) + \left(\frac{\gamma\theta}{K} - \frac{n}{x}\right)^2 J_n^2(x)\right]\frac{\sin^2 N\pi(\omega/\omega_c - n)}{(\omega/\omega_c - n)^2} \tag{3.7}$$

where J_n is the Bessel function and J_n' its derivative, the index n corresponds to the order of the harmonic. It is also important to note that, unlike the expression for the sinusoidal trajectory this one takes the number of periods on the trajectory, N, into account. Furthermore, Equation (3.7) is only valid for $N \gg 1$. Both the critical frequency ω_c and the variable x have different definitions in this context:

$$\omega_c = \frac{2\gamma^2\omega_\beta}{1 + K^2 + \gamma^2\theta^2}\,, \qquad x = \frac{K\omega\theta}{\gamma\omega_\beta}\,. \tag{3.8}$$

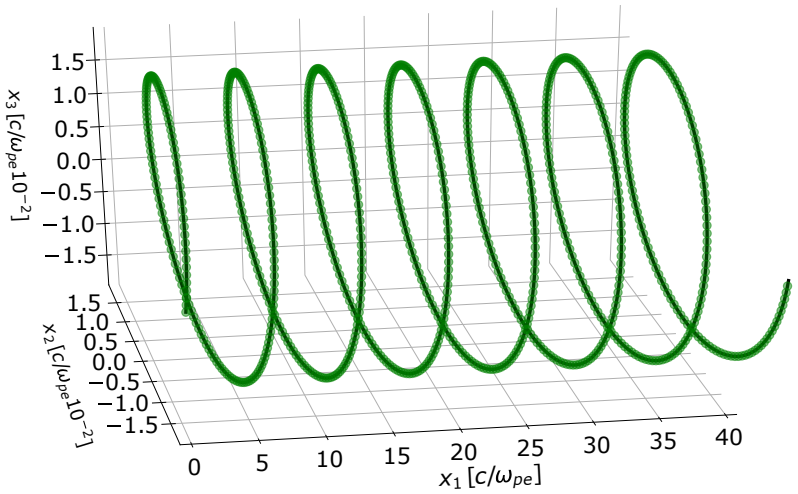

Figure 3.9: Helical trajectory of the particle. Relativistic particle undergoing a circular motion on the x_2x_3 plane while moving forward in the x_1 direction. $\gamma = 100$.

The angle integrated frequency spectrum is given by:

$$\frac{dI}{d\omega} = \frac{4\pi N q_e^2 K^2 r}{c} \sum_{n=1}^{+\infty} \left[J_n'^2(x_n) + \left(\frac{\alpha_n}{K} - \frac{n}{x_n} \right)^2 J_n^2(x_n) \right] H(\alpha_n^2)\,. \tag{3.9}$$

Here, the new variables r, α_n and x_n are introduced: $r = \omega/(2\gamma^2\omega_0)$ is a scaled frequency, and $\alpha_n = \sqrt{n/r - 1 - K^2}$ and $x_n = 2Kr\alpha_n$ are auxiliary variables. H is the Heaviside step function.

The frequency integrated angular spectrum is given by:.

$$\frac{dI}{d\Omega} = \frac{N q_e^2 \omega_\beta K^2}{c} \frac{8\gamma^4}{1 + K^2 + \gamma^2\theta^2} \sum_{n=1}^{+\infty} n^2 \left[J_n'^2(x_n) + \left(\frac{\gamma\theta}{K} - \frac{n}{x_n} \right)^2 J_n^2(x_n) \right]\,. \tag{3.10}$$

A detailed derivation of these expressions may be found in Kincaid's original paper [26]. Moreover, in what concerns the K parameter, two distinct regimes can be identified: smaller K's are found in tighter orbits where the pitch angle, $\psi_b = K/\gamma$, is smaller than the radiation cone aperture, $1/\gamma$, resulting in a single radiation cone and an angular spectrum with an on-axis maximum, as can be seen in the left-hand side of Figure 3.10. Higher K's are found of trajectories with higher pitch angle which becomes higher than the radiation cone aperture, resulting a radiation conical surface with an on-axis dip (right-hand side of Figure 3.10).

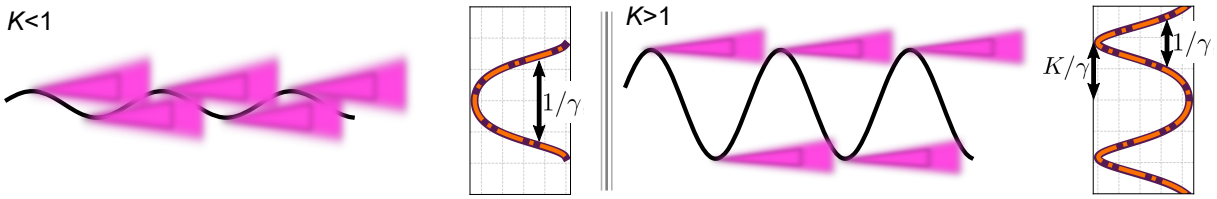

Figure 3.10: Illustration of the effect of the K parameter. Smaller K's as presented in the left trajectory are the result of a tight helix, whereas bigger K's are associated with higher amplitude helices. The angular spectrum at the detector is represented besides both trajectories.

As the expressions given above are valid for a generic K, we benchmarked the code's results against predictions for both $K < 1$ and $K > 1$, taking into account that for higher K's, the spectrum contains more harmonics, which affects the order at which the summation on Equations (3.7) through (3.10) are

truncated.

3.2.1 Benchmark for $K = 0.8$

Using the trajectory of an electron with $\gamma = 57.3$ undergoing an helical motion with amplitude $r_b = 0.014\, c/\omega_p$ and frequency $\omega_\beta = 1\,\omega_p$ ($K = 0.8$), we were able to benchmark the diagnostic against Equation (3.7). As before, the spherical detector lied on the x_3x_1 plane with a radius of $10^5\, c/\omega_p$ and angular aperture of 0.03 rad (512 cells). Its temporal resolution was $1.33 \times 10^{-5}\, \omega_p^{-1}$.

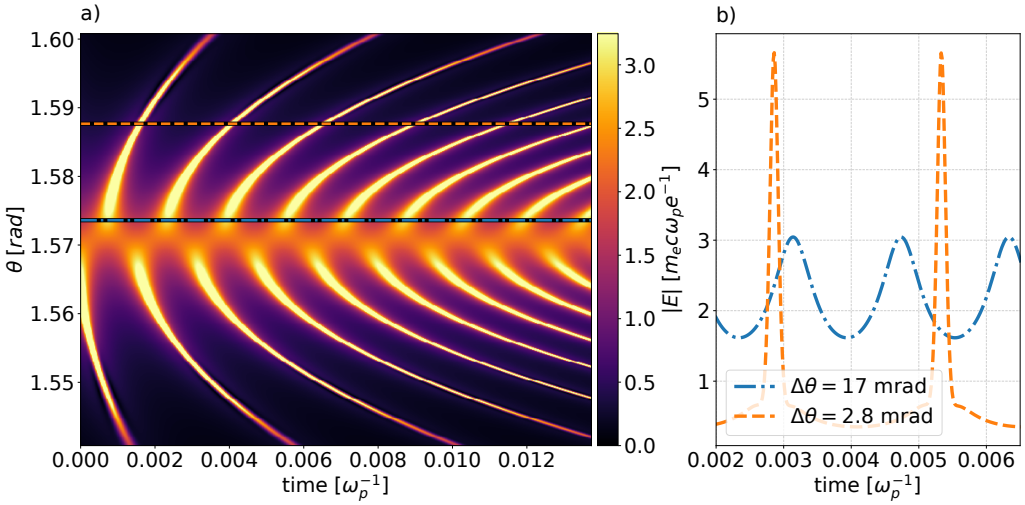

Figure 3.11: a) Spatiotemporal profile of the magnitude of the electric field at the spherical detector. b) Temporal zoom of the lineouts of the spatiotemporal profile. The vertical axis of panel b) and the color bar of panel a) share the same units.

The spatiotemporal signature of the detected field (Figure 3.11) evidences an interesting, albeit expected, feature: the maximum intensity radiation is located around the axis with a small drop in the field intensity on-axis, resembling the expected intensity cone of the previous discussion. Another interesting aspect of the spatiotemporal profile is the distribution of the radiation structures. Similarly to the sinusoidal case, these structures feature a parabolic shape, however, these parabolae are broader at the axis and become thinner as θ moves away from $\pi/2$, as evidenced by the lineouts on the panel b) of Figure 3.11. The cause for this is deeply linked with the spectrum, as the number of harmonics varies drastically with the angle θ, as shown in panel a) of Figure 3.12. In fact, higher deviations from the axis result in a signal with more harmonics and, therefore, composed by thinner peaks.

The spectrum, which is supposed to be symmetric around the axis ($\theta = \pi/2$), was obtained from the simulation results through an FFT. Panel a) on Figure 3.12 shows the direct comparison between simulation and theory in the same manner as Figure 3.5. The lineout at $\Delta\theta = 0.02$ rad shows a perfect match between the harmonics present in both spectra, with a significant difference in the noise of both spectra, as the theoretical prediction features a much higher noise baseline, which is due to the truncation of the summation of Equation (3.7).

As for the integrated spectra, shown on panels c) and d) of Figure 3.12, a much better agreement can be found with the frequency-integrated spectrum, d), than with the angle-integrated spectrum, c), but the overall agreement is very good. In addition to matching the theoretical prediction perfectly, the frequency integrated spectrum ($dI/d\Omega$) confirms the expectations for the intensity profile when $K < 1$,

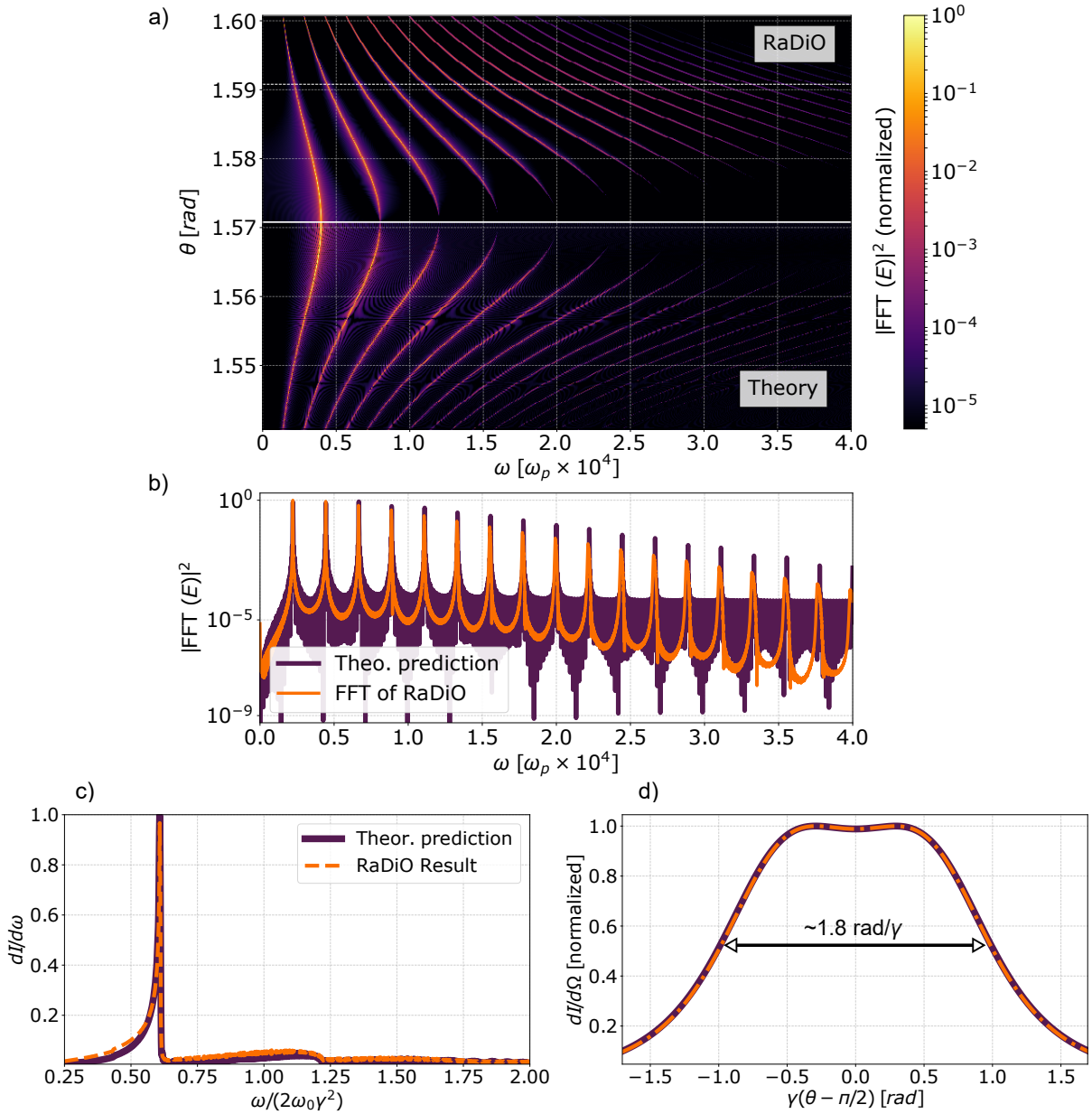

Figure 3.12: a) Comparison between the theoretical expectations for the radiated spectrum and the Post-processing code results for the radiated spectrum for $K = 0.8$. b) Comparison between a lineout at $\Delta\theta = 0.02$ from both spectra. Panels c) and d) feature the comparison between the angle and frequency integrated spectra, respectively.

featuring an accumulation of intensity near the axis albeit with a slight dip caused by the fact that K, despite being smaller than 1 ($K = 0.8$), is still close to the unity.

Additionally, this accumulation of radiation can be found inside a cone with aperture of about $1.8\,\gamma^{-1}$ rad (Full Width at Half Maximum), instead of the expected $1\,\gamma^{-1}$ rad for $K < 1$, however, with $K = 0.8$ close to 1, this case is a transition between both regimes. In the $K > 1$ the pitch angle must be taken into account, which would lead to a total aperture of $1\gamma + 2K/\gamma = 2.6\gamma^{-1}$, the measured aperture was $1.8\,\gamma^{-1}$rad which corresponds to average of the expected aperture of both regimes.

3.2.2 Benchmark for $K = 2$

With a variation of the trajectory analyzed in the previous section, this time with a larger amplitude helix, $r_b = 0.02\, c/\omega_p$, and $\gamma = 100$ but with the same frequency, $\omega_\beta = 1\omega_p$, we obtained an helical trajectory with $K = 2$. For this benchmark, we used the same detector, which lied on the x_3x_1 plane with a radius of $10^5\, c/\omega_p$ and angular aperture of 0.03 rad. The detector had a temporal resolution of $1.33 \times 10^{-5}\, \omega_p^{-1}$.

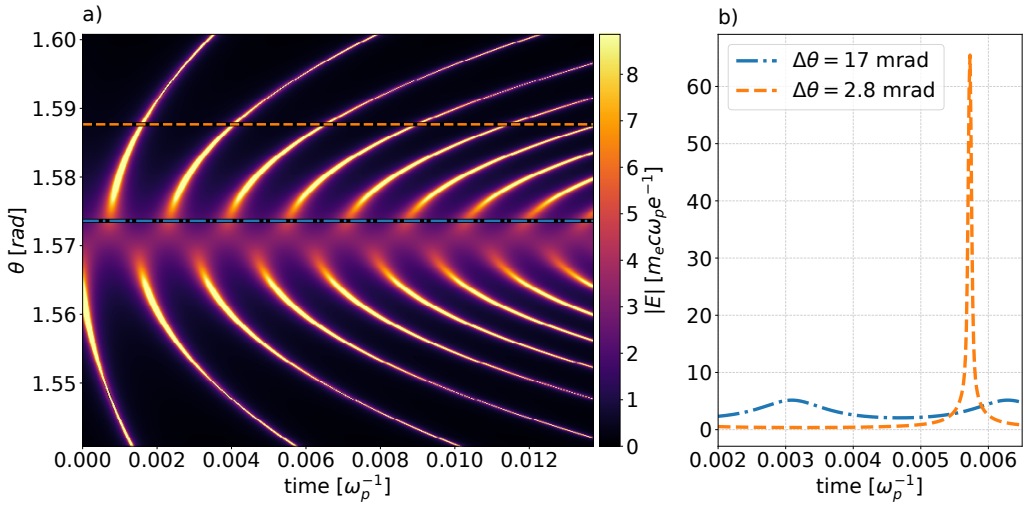

Figure 3.13: a) Spatiotemporal profile of the magnitude of the electric field at the spherical detector. b) Temporal close-up of the lineouts of the spatiotemporal profile. The vertical axis of panel b) and the color bar of panel a) share the same units

The spatiotemporal signature of the detected field is displayed on Figure 3.13, this time, it is clear that the maximum intensity radiation is located off-axis, displaying a significant drop in the field intensity on-axis, resembling the expected intensity profile of Figure 3.10. The parabolic structures that erupt from the axis are once again broader on-axis, and become thinner for higher apertures, as evidenced by the lineouts of Figure 3.13(b). The reason for this effect, discussed in the previous section may be further confirmed with panel a) of Figure 3.14.

Once again, the spectrum was obtained from the simulation results by performing a temporal FFT on the electric field's components and the comparison with the theoretical results was made by placing the two complementary halves of the detector on top of each other (panel a of Figure 3.14). As before, both plots mirror each other almost perfectly, as they are supposed to do. There is, nevertheless, a slight difference for higher frequencies, as the simulated spectrum seems to have some extra harmonics, as evidenced by the dark region on the bottom-right part of the plot in opposition to the bright region on the upper-right part of the plot. This is, in fact, a mismatch, however, the problem does not lie on the extra harmonics of the simulated spectrum but the missing harmonics in the theoretical spectrum, which are caused by the truncation of the summation on the theoretical expression (Equation (3.7)). In this case, the summation was carried out until $n = 55$, however, for $K = 2$ the spectrum is composed by much more harmonics which only appear on the simulated spectrum.

The lineout at $\Delta\theta = 0.02$ (panel b of Figure 3.14) shows a perfect agreement between the frequencies of the harmonics of both results, however, the same cannot be said about the harmonics' amplitudes, as the ones from the theoretical prediction seem to vary periodically, whereas the ones from the simulated spectrum appear to remain relatively constant.

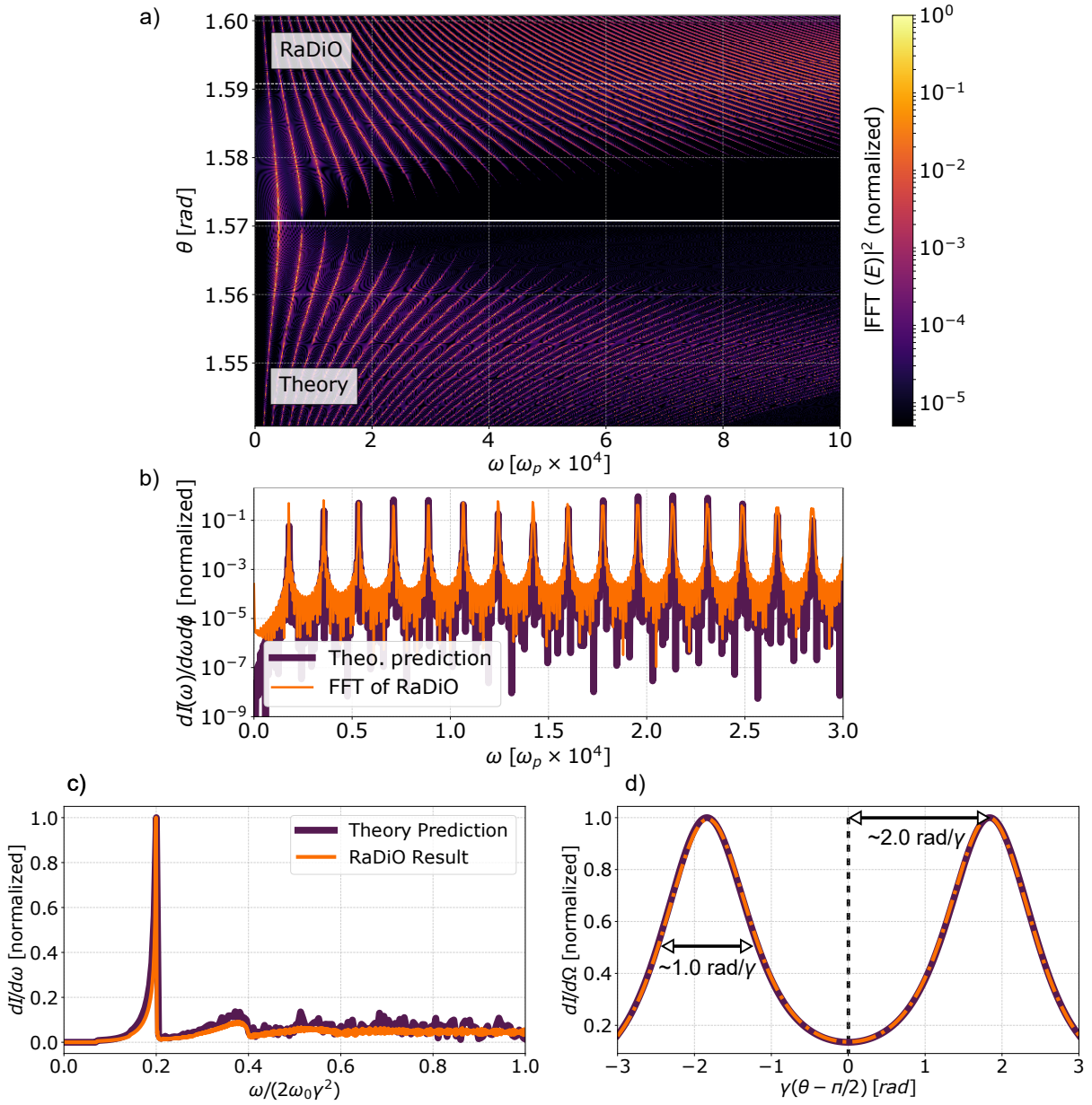

Figure 3.14: a) Comparison between the theoretical expectations for the radiated spectrum and the Post-processing code results for the radiated spectrum for $K = 2$. b) Comparison between a lineout at $\Delta\theta = 0.02$ from both spectra. Panels c) and d) feature the comparison between the angle and frequency integrated spectra, respectively.

The integrated spectra once again corroborate the assertion that the simulation results match the theoretical expectations, as the simulated spectra follow the theoretical lines very closely, with a better agreement on the frequency integrated angular spectrum (panel d of Figure 3.14). Moreover, this angular spectrum further validates the prediction of Figure 3.10 for $K > 1$, as it features two maxima considerably off-axis, near $\theta = K/\gamma = 2\gamma^{-1}$ rad, as well as very pronounced minimum on-axis. The aperture of each peak is also in agreement with the expected $1\gamma^{-1}$ rad.

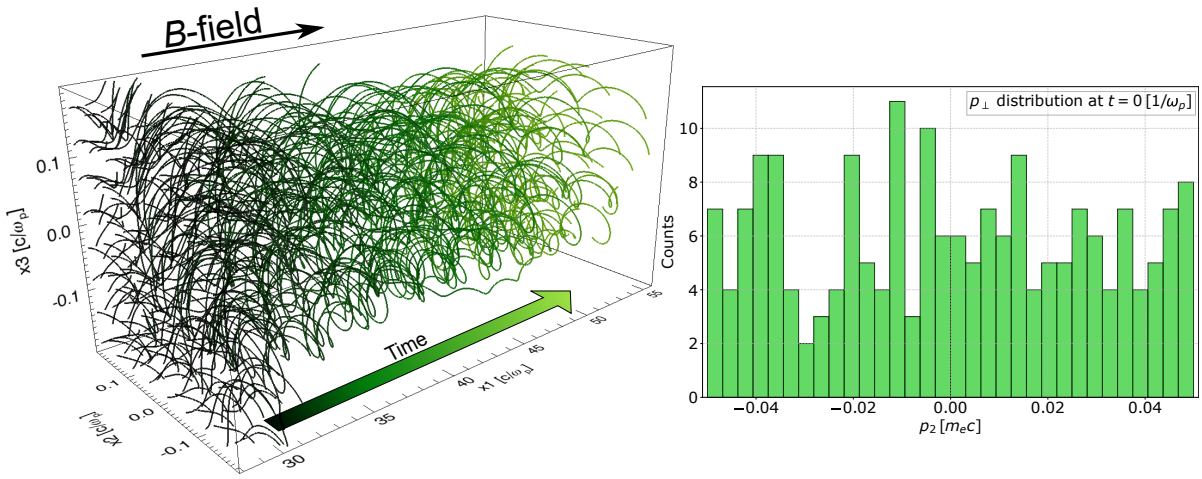

Figure 3.15: 3D trajectories of the 192 particles (left). Initial distribution of the transverse momenta of the particles (right).

3.3 Benchmarking the run-time version of RaDiO

The benchmarks described in the previous sections were performed using the post-processing version of the code, which calculates the radiation from previously obtained trajectories, either from simulation or other sources. These tests confirmed the accuracy of the method and established the post-processing code's results as reliable.

Despite the similarities, the run-time counterpart of code, that runs at the same time as the OSIRIS simulation progresses, is a different code altogether. Therefore, it needs to be benchmarked as well. Given that the post-processing code was previously benchmarked against multiple theoretical predictions, we needed only to prove that, in the same conditions, both codes return the same results, that is, we needed to benchmark the run-time version against the post-processing version.

For that purpose, we ran a simple OSIRIS 3D simulation with the run-time radiation code, and then used the trajectories from this run on the post-processing version. Finally, we compared the results of both codes. The simulation contained a single species of radiative species initially bound to a sphere. The 192 particles of this species were initialized with uniform velocity along a given direction (henceforth called the *longitudinal direction*) and random perpendicular velocity shaped by the *waterbag* function. A uniform longitudinal magnetic field made the particles undergo a radiation favorable helical trajectory as displayed on Figure 3.15. The simulation parameters are listed in Table 3.1:

The radiation from these particles was captured using a spherical detector with one spatial dimension

Table 3.1: Beam and box parameters. Indices 1, 2 and 3 refer to the 3 spatial directions

Species parameters		**Box parameters**	
Sphere Center	28.2, 0.,0. c/ω_p	Box Dimensions (L_1, L_2, L_3)	40, 0.4, 0.4 c/ω_p
Radius	0.5 c/ω_p	No. Cells (n_1, n_2, n_3)	100, 8, 8
Momentum (p_1)	1.0 $m_e c$	Time step	0.01 ω_p^{-1}
Momentum (p_2)	-0.05$< p_2 <$0.05 $m_e c$	Simulation Time	40.2 ω_p^{-1}
Particles p/ cell	1,1,1		

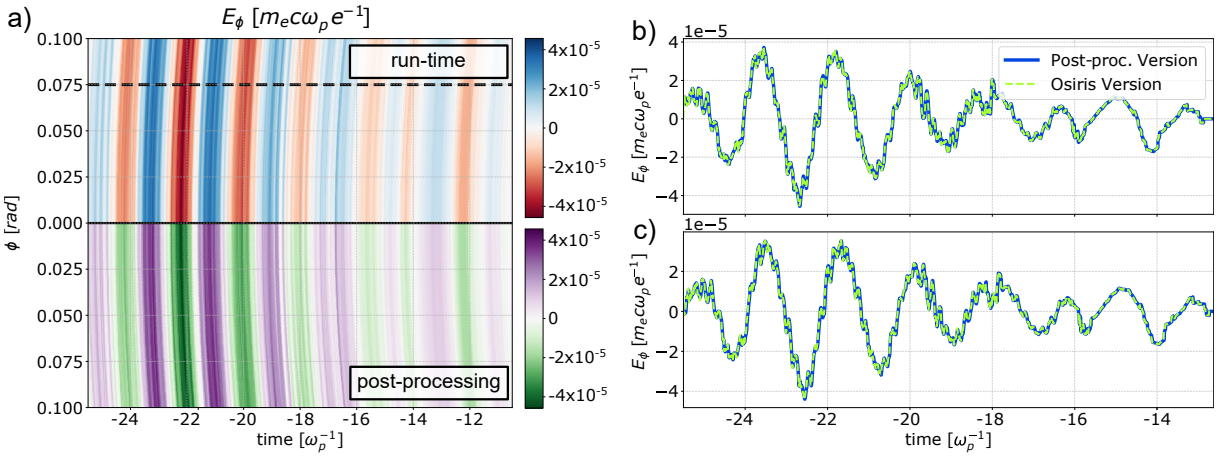

Figure 3.16: Comparison between the results of post version of the code. a) Full spatiotemporal detectors, mirrored. b) Lienout at $\phi = 0$. c) Lineout at $\phi = 0.075$.

and one temporal dimension placed at $R = 10^5\, c/\omega_p$, $\theta = \pi/2$ rad, and with ϕ ranging from 0 to 0.1 rad (1024 cells). This detector had 4096 temporal cells ranging from $t = R/c - 25.5\,\omega_p^{-1}$ to $t = R/c - 0.5\,\omega_p^{-1}$.

The results from both simulations are displayed in Figure 3.16. Panel a) contains the full spatiotemporal signature left on both the run-time (upper half) and the post-processing (lower half) detector. The lower plot features an inverted vertical scale so that its image mirrors the one from the upper plot, making the comparison easier. As a result, the similarity between the results from both codes becomes evident as result from both versions seem to mirror each other, the only difference being the color scheme. Moreover, the broad parabolic structures in the spatiotemporal detector feature some ridges which are further evidenced in the lineouts at the right, where small amplitude perturbations coming from low energy particles that alter the shape of the radiation left at the detector by the higher energy particles.

The lineouts at $\phi = 0$ rad (panel b) and $\phi = 0.075$ rad (panel c) further confirm the agreement between both versions of the code and ultimately lead to the conclusion that the results coming from the run-time version are equally reliable and can be used to accurately simulate radiation emission processes in plasma environments.

3.4 Performance and Scalability

3.4.1 Performance

In PIC codes, the number of operations per iteration scales roughly with $N_p + N_g$, with N_p the number of particles in the simulation and N_g the number of grid cells. The radiation algorithm requires an extra set of operations per particle per detector spatial cell at each iteration, increasing the number of operations to something of the order of $N_p + N_g + N_{det}N_{rad}$, where N_{det} is the number of detector spatial cells and N_{rad} is the number of radiative particles.

This rough estimate can be very useful when we are interested in a general idea of how much longer than a standard OSIRIS simulation will a run with the radiation diagnostic take. However, apart from the fact that this assertion lacks validation, as other factors such as communications (as seldom as they

may occur) might contribute to the run time, a more precise estimate is often needed. In this way, we ran several performance tests with the aim of discovering the actual influence of detector's size and number of radiative particles on the simulation's run time.

For that purpose, we ran ultra high resolution 3D simulations of laser-plasma interactions in a Thomson scattering scenario. The computational load was varied by either increasing the number of cells in the detector or the particles per cell of the radiative species. The simulations consisted in counter-propagating beams of electrons and light and their global parameters are listed in Table 3.2

Table 3.2: Performance simulation parameters. Indices 1, 2 and 3 refer to the 3 spatial directions.

Box parameters		**Beam Parameters**	
Box Dimensions (L_1, L_2, L_3)	240, 0.02, 0.02 c/ω_p	p_1 (E-beam)	-100 $m_e c$
No. Cells (n_1, n_2, n_3)	2400, 240, 240	ω_0 (Laser)	1 ω_p
Time step (dt)	0.01 ω_p^{-1}	a_0 (Laser)	1
Simulation Time	300 ω_p^{-1}		

The spherical detector was placed far from the simulation domain in the negative x_1 direction ($R = 10^6\, c/\omega_p$), with $\theta = \pi/2$ rad and ϕ ranging from 3.1 to 3.18 rad. It acquired radiation from $t = R + 202.22\,\omega_p^{-1}$ to $t = R + 202.24\,\omega_p^{-1}$ with 16635 temporal cells. The number of spatial cells of this detector was varied from 0 to 128 and the number of particles was kept constant at 32840 while the simulation was run for 408320 time steps.

The performance runs were performed at SuperMUC, the Leibniz Supercomputing Centre's supercomputer [27], currently ranked at place 57 in the top 500 [28], using a maximum of 4096 cores. The results are summarized in Figure 3.17, where the run times were adjusted to a straight line via through a linear regression in order to find their dependence with the number of cells in the detector and number of particles.

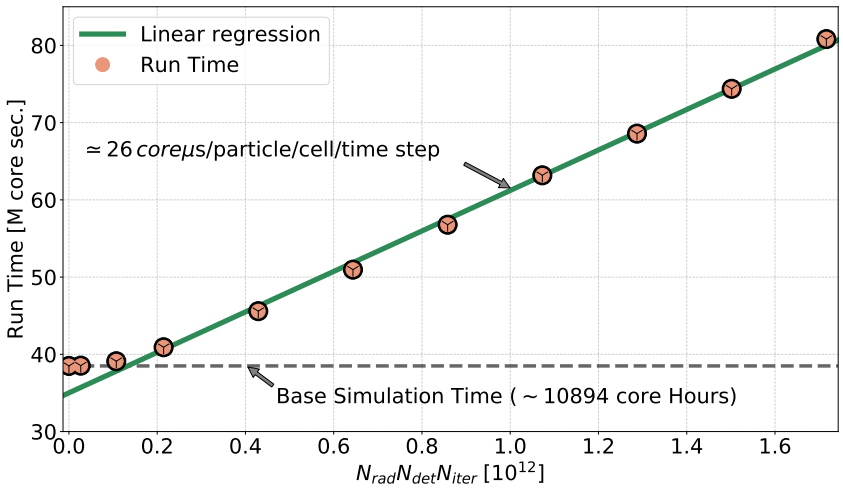

Figure 3.17: Result of the performance runs at SuperMUC. The dashed line represents the baseline simulation time for runs without radiation.

This figure confirms the assertion that the run-time should increase linearly with $N_{rad}N_{det}$ and quantifies the rate at which it increases: 26 CPUμs/particle/detector cell/iteration. This value is higher than

the one obtained for standard optimized OSIRIS simulations (with no radiative particles), reported to be of less than 1 CPUμs/particle/iteration, this disparity is caused by two main factors: first, unlike most of the OSIRIS code, the radiation is not optimized for vector parallel computing, which explains some decrease in performance, and secondly, despite all the efforts to optimize the radiation code, there is an inefficient section of the algorithm that cannot be avoided: after computing the time of arrival, the algorithm checks if that time falls into the detector's timespan, this requires that an *if* statement be present in the innermost loop, which is an inefficient implementation.

Additionally, it is interesting to note that the simulation's run times don't always follow the linear regression, in fact, for a small enough detector (*i.e.* the first three points of the plot), the number of grid cells N_g is still the major contribution for the number of operations.

3.4.2 Scalability

OSIRIS is a highly scalable code that has shown incredible performance in some of the world's largest supercomputers [29]. Therefore, in order to guarantee that this diagnostic is suitable for the OSIRIS framework it is necessary to assess its scalability.

For that purpose, we ran a strong scaling test with the run-time diagnostic. Strong scaling tests evaluate how the code's parallel efficiency behaves when the same simulation is split among more processing units. The tests consisted in running a 2D simulation of a single radiative species with uniform density and thermal velocity with a spherical detector with 1024 spatial cells. The most relevant simulation's parameters are summarized in Table 3.3:

Table 3.3: Scalability simulation parameters. Indices 1, 2 and 3 refer to the 3 spatial directions.

Box parameters		**Species Parameters**	
Box Dimensions (L_1, L_2)	10, 10 c/ω_p	Particles p/ Cell	3×3
No. Cells (n_1, n_2)	400, 400	$\mathbf{p}_{th}$ (p_1, p_2, p_3)	1.0, 1.0, 1.0 $m_e c$
Time step (dt)	0.0169 $1/\omega_p$		
Simulation Time	90 $1/\omega_p$		

The tests were performed at the IST Cluster, a 1560 core system in IST, where the same simulation was ran with a number of cores ranging from 40 to 640. The parallel efficiency is defined as the ratio between the speedup, T_N/T_0, and the amount of extra cores used, N/N_0, leading to $\eta_N = T_N N_0/NT_0$, where the index 0 refers to the run with the least amount of cores, which in this case is 40 cores.

Using 40 cores, running the same OSIRIS simulation with radiation takes about 150 times more time than running it without radiation, this means that the contribution from number of particles dominates over the contribution from the number of grid cells, and by using 1024 detector cells we are mainly testing the scalability of the radiation algorithm.

The results are shown in Figure 3.18, it is evident that the parallel efficiency decreases with the amount of cores used, reaching a minimum of about 87% for 640 cores. This decrease is most likely caused by the increasing amount of communications that come with high core counts, despite the fact

that the communications involving the detector object happen very rarely. Additionally, particle communications happen very often in PIC codes, especially in simulations with warm plasmas. As the particles of the radiative species contain more information (previous positions and momenta), the communications for such objects take longer.

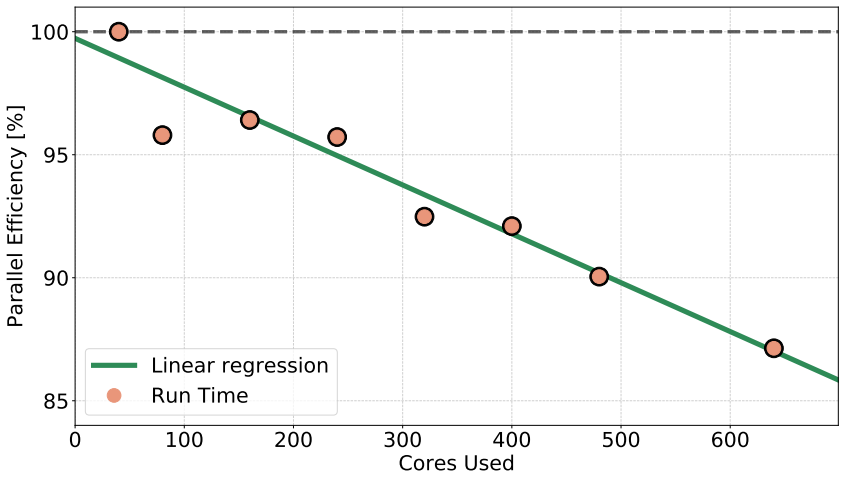

Figure 3.18: Scalability test performed at the IST cluster. The dashed line represents the ideal scenario where no efficiency is lost by increasing the number of cores.

Chapter 4

Production RaDiO Simulations

After the successful benchmarks of the previous chapter, the radiation diagnostic for OSIRIS was ready to be used in production scenarios.

4.1 Radiation in Plasma Wakefield Acceleration

Conventional radio-frequency accelerators comprise several individual accelerators that accelerate the moving particles by applying a synchronized electric field. The energy gained by the particle in these devices is directly linked to the voltage applied to each individual accelerating unit, which is limited by the electrical breakdown [30], a phenomenon that consists in a flow of current through the accelerating chamber caused by a high enough voltage. This limits the amount energy that each individual accelerator can provide to the particle, however, if a great number of these devices are linked in series, energy gains of the order of 7 TeV can be obtained [31]. The drawback of this solution is the high number of individual accelerators needed in order to obtain a decent energy gain render the overall structure both extremely expensive and sizable.

Plasma based accelerators emerged as a compact alternative to these machines, as in these media the maximum field is no longer restrained by the electric breakdown limit and higher accelerating fields and energy gains are possible. The underlying mechanism was first proposed by Tajima and Dawson [32] in 1979, it consists in using a short and intense laser pulse to generate a plasma wave moving at almost the speed of light that is capable of pushing the plasma's electrons away form the pulse, creating a positively charged region, the so called ion channel, as shown in Figure 4.1 which illustrates Laser Wakefield Acceleration (LWFA). Two types of fields tend to appear in this region: the acceleration field and the focusing field.

The acceleration field appears on the longitudinal direction and is caused by the charge separation that appears behind the the ion channel when some of the electrons that were pushed away move back to their original positions. This field is capable of accelerating any particles that are trapped inside the ion channel and is displayed on panel b of Figure 4.1.

The focusing field, transverse to the laser's motion, exerts a restoring force on the particles, trapping

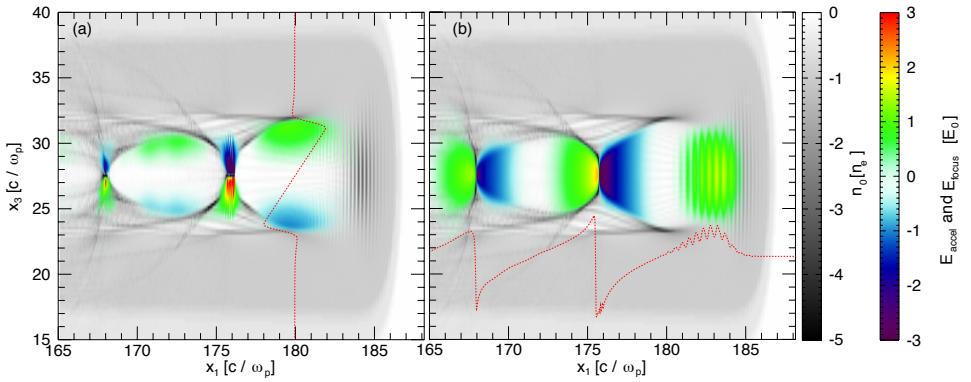

Figure 4.1: Snapshot of a 2D LWFA simulation. The plasma species density is represented in grayscale. Panel a) displays the transverse focusing field in the plasma region together with a lineout. Panel b) displays the longitudinal acceleration field in the plasma region together with a lineout. The laser beam is propagating from left to right.

them inside the ion region. It can be roughly calculated in cylindrical geometry in 3D using Gauss's law [33] and is given by:

$$\mathbf{F_{res}} = -m\omega_p^2 \mathbf{r}_\perp / 2 \tag{4.1}$$

where $\mathbf{r}_\perp$ is the radial position of the particle and m is its mass. Although the geometry is different in 2D, the same phenomena occurs as illustrated if the panel a of Figure 4.1. This force is responsible for the oscillatory motion (the so-called the betatron motion) of the charged particles in this region that results in a sinusoidal-like trajectory. However, as the particle may be subjected to acceleration the period and amplitude of the trajectory may vary with time [34]. Nevertheless, the particles undergoing such trajectories are expected to produce radiation with interesting and unknown spatiotemporal properties.

LWFA uses a laser pulse as the wake driver. However, it is also possible to use a highly energetic electron, proton or positron beam to drive the plasma wake in a process called Plasma Wakefield Acceleration (PWFA).This process is illustrated Figure 4.2, which shows the wake generated by an electron beam. This method, proposed by Chen et al. [35] in 1985, can be more desirable than LWFA as with current technology, particle beams are capable of holding more energy than laser beams and, therefore, capable of yielding much higher energy gains the LWFA. Over the past few years, numerous experiments have been conducted in order to provide the proof of concept for this method, some with impressive results such as the doubling of energy of a 84 GeV electron beam to 84 GeV in a 84 cm plasma [9].

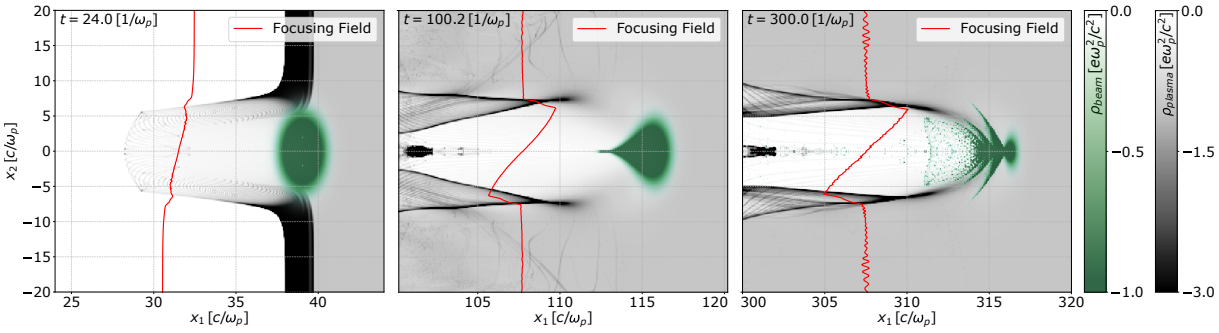

Figure 4.2: Multiple snapshots of a 2D PWFA simulation. The plasma species density is represented in grayscale. The laser beam is propagating from left to right and its density is represented by the green scale. A lineout of the focusing field is shown at each instant.

4.2 Full Beam Radiation in PIC

With the aim of capturing the undiscovered spatiotemporal signature of the radiation emitted in PWFA scenarios, we ran several 2D simulations in OSIRIS using the radiation diagnostic developed in this thesis, with particular interest in the radiation emitted by the driving electron beam. This is the beam that delivers energy to the plasma wake so some deceleration is expected.

These simulations followed two different species: a highly energetic electron beam with a Gaussian density profile and the uniform plasma target in which it enters and travels, as shown in Figure 4.2. In order to accomplish this, a moving window in x_1 was used, this means that the simulation box moved with the speed of light along x_1, the propagation direction of the electron beam.

The electron beam density profile was defined using Gaussian functions:

$$n_{beam}(x_1, x_2) = 2.0 \times \exp\left[-\frac{(x_1-\mu_1)^2}{\sigma_{\parallel}^2}\right] \exp\left[-\frac{(x_2-\mu_2)^2}{\sigma_{\perp}^2}\right] n_0, \tag{4.2}$$

Using the parameters listed on Table 4.1 with 1 particle per cell (ppc) in each direction, the electron beam contained a total of 10500 simulation particles. In some simulations, the electron beam species was split in two subgroups, so that only a fraction of the particles in the beam would be of radiative type. This trick was fairly useful when we intended to isolate the radiation emitted by different parts of the beam. Additionally, the beam was initialized with a purely longitudinal relativistic momentum, $\mathbf{p} = \gamma m v_1 \mathbf{e_{x_1}} = p_1 \mathbf{e_{x_1}}$, with $p_1 = 1000.0\, m_e c$. The plasma target had a uniform density $n_p = 1.0\, n_0$ with 2 ppc in each direction and occupied a bounded region. Table 4.1 lists the simulation parameters.

Table 4.1: Beam, plasma and box parameters for Plasma Wakefield acceleration. The indices 1 and 2 refer to the horizontal ($\parallel$) and vertical ($\perp$) direction, respectively.

Beam/plasma parameters		**Box parameters**	
Beam σ ($\sigma_{\parallel}^2$, $\sigma_{\perp}^2$)	2.0, 30.0 c^2/ω_p^2	No. Cells (n_1, n_2)	200, 300
Plasma Density	1.0 n_0	Time step	0.09 $1/\omega_p$
Plasma Bounds	$x_1 > 30\, c/\omega_p$	Simulation Time	900 $1/\omega_p$
	$-30 < x_2 < 30\, c/\omega_p$		

The emitted radiation was captured with a spherical detector placed far from the simulation domain in the x_1 direction ($R = 10^6\, c/\omega_p$). It consisted in an spherical slice located in the $x_2 x_1$ plane facing the x_2 axis, *i.e.* $\theta = \pi/2$ rad and ϕ spanning from -0.1 to 0.1 rad with 1024 cells as illustrated in Figure 4.3.

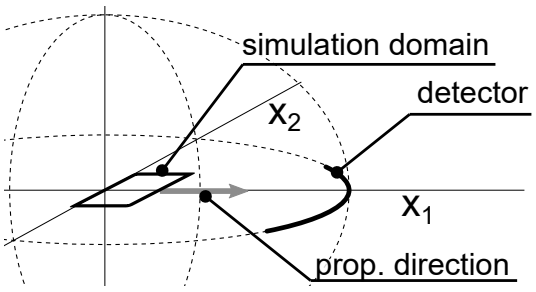

Figure 4.3: Illustration of the PWFA RaDiO simulation set-up.

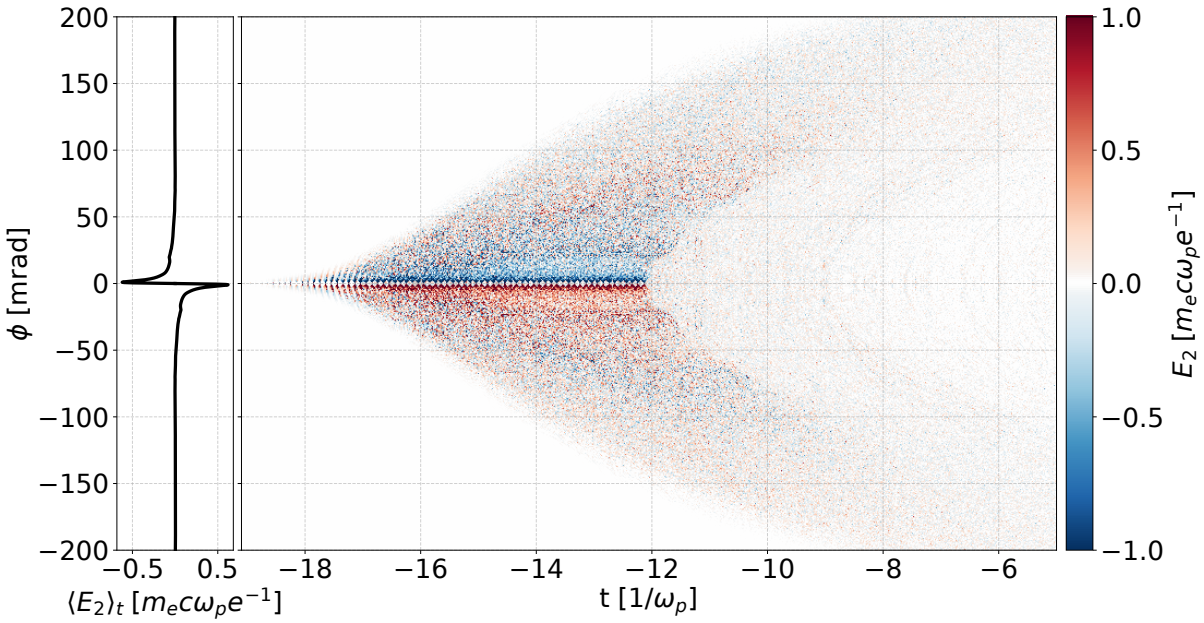

Figure 4.4: Full spatiotemporal profile of the radiation emitted by the full electron beam along the transverse direction. The time averaged field is shown on the left plot

The results for a time interval between $t = R/c - 19.1\,\omega_p^{-1}$ and $t = R/c - 5.0\,\omega_p^{-1}$ with 8192 temporal cells are shown on Figure 4.4. In this figure we see a clear separation at $\phi = 0$ as it seems that the transverse field, E_2 transitions from being mostly positive for $\phi < 0$ to being mostly negative for $\phi > 0$. This fact is evidenced by the time averaged field, plotted on the left, which shows a perfectly symmetric field with respect to ϕ, with an accumulation of positive values for $\phi < 0$ and an accumulation of negative field values for $\phi > 0$. This suggests that a particle placed in that region would experience a net transverse acceleration when subject to this radiation. This is a purely spatiotemporal result and further evidences the importance of a spatiotemporal approach. To the best of our knowledge, this effect has not yet been tested and the actual implications of this result on the particles motion is still unexplored and requires a more profound study.

Furthermore, the parabolic signatures explained in section 3.1 appear as expected in the spatiotemporal profile. However, the emitted beam of light features a distinct tail for earlier times which corresponds to radiation emitted by the front end of the electron beam. Due to the Gaussian profile there are less particles in that region so the constructive interference is weaker for the radiation emitted in less dense regions. Therefore, given that the intensity of the radiation along these parabolae decreases with the distance from the axis, the parabolic structures tend to spread to wider angles for radiation emitted in the central region where there are more particles, and tend to be confined to narrower angles for radiation emitted in the peripheral region of the beam, where there are less particles, creating the aforementioned tail.

This line of thought seems to suggest that there should be two tails, corresponding to the two ends of the electron beam. However, Figure 4.4 shows only one tail, this happens because the radiation from the front end of the beam arrives earlier than the radiation from the back end of the beam, therefore, the tail that corresponds to the back end of the beam is hidden behind the radiation from the rest of

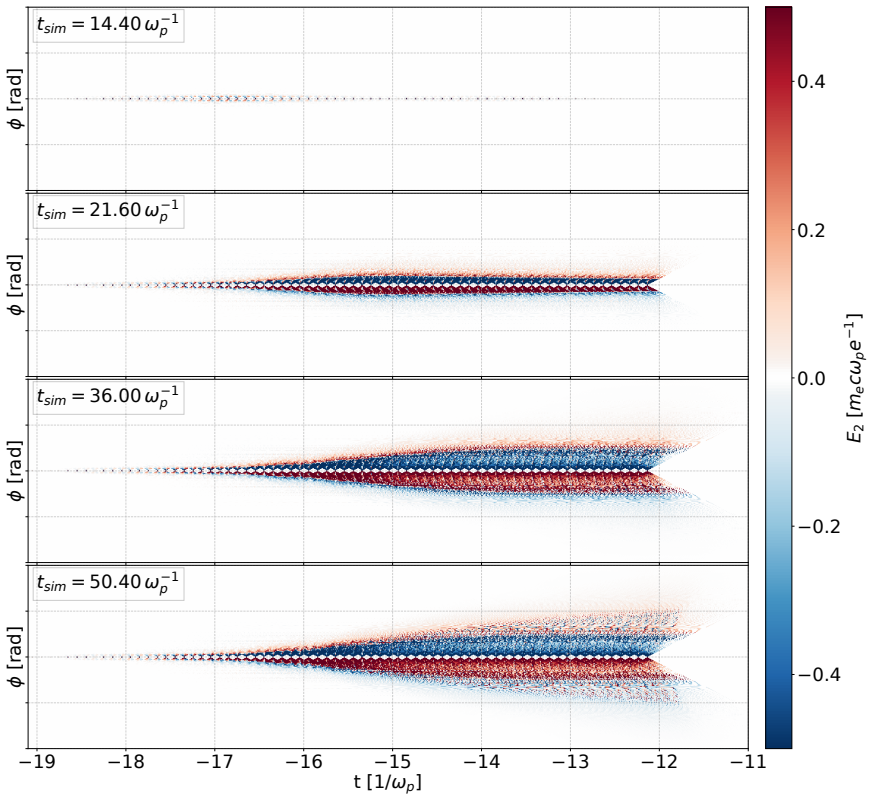

Figure 4.5: Full spatiotemporal profile of the radiation emitted by the full electron beam along the transverse direction at different instants of the PIC simulation. ϕ ranges from -0.1 rad to 0.1 rad.

the beam, whereas the tail that corresponds to the front end of the beam can be clearly observed in Figure 4.4. This assertion is corroborated by the results shown on Figure 4.5. This figure shows the evolution of the spatiotemporal profile at the detector for the early stages of the PIC simulation, in it, we can clearly observe an initially faint distribution of radiation with an accumulation near the center and featuring the two tails (as expected, due to the gaussian nature of the beam). In the following time steps, this central accumulation of radiation starts building up and spreading to later times, gradually erasing any signs of the second tail.

By using a detector with a shorter, but better resolved timespan, that captured radiation from $t = R/c - 15.3\,1/\omega_p$ to $t = R/c - 14.6\,1/\omega_p$, with 16384 temporal cells, we were able to acquire some more knowledge about the spatiotemporal signature of the emitted radiation. Figure 4.6 shows this close-up of the detector on-axis at different times in the simulation. The first structures that appear on the detector are these periodically located X shaped accumulations of radiation, whose period corresponds to the cell size in the x_1 direction, leading to the conclusion that each of these structures corresponds to radiation emitted by particles in the same vertical slice of the beam.

Upon a closer inspection, it is clear that these structures are a set of radiation parabolae with maximum intensity on axis, each of them possibly comes from a different particle in the same vertical slice. As the simulation progresses, and the beam particles perform more and more oscillations, new emissions start filling the gap between the aforementioned structures. However, as the beam moves through the plasma, its particles start to drift apart and the radiation they emit no longer interferes constructively, resulting in less intense radiation.

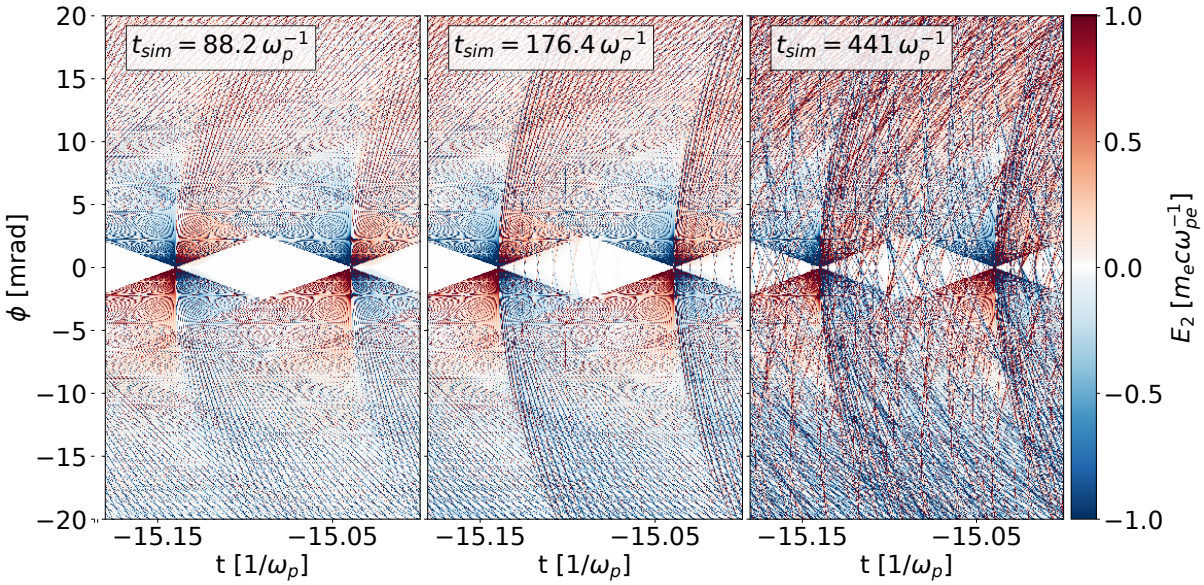

Figure 4.6: Close-up of Figure 4.4 with higher resolution at several stages of the simulation.

The genesis of the X shaped structures can be well understood by analyzing the signature left by two particles placed symmetrically with respect to the x_1 axis, for that purpose, we added a third species to the simulation. This species was of the radiative type, and contained two particles that were inserted into the electron beam. The corresponding particles on the beam species were removed.

The resulting spatiotemporal profile can be found on panel b) of Figure 4.7, This plot contains radiation emitted by the two particles initialized at $\mathbf{x} = (15,\, 3)\, c/\omega_p$. In it, it is made clear that the X shaped structure is, in fact, the superposition of symmetric parabolic structures left by both particles. Panel a) shows the same detector in a similar scenario, the only difference being the initial position of the particles which were initialized closer to the x_1 axis, but in the same vertical slice, at $\mathbf{x} = (15,\, 2)\, c/\omega_p$, the results are very much alike, however, the parabolic structures appear to be narrower in this case. The results from these two examples confirm that the X shaped structures are the result of the superposition of the first radiation emitted by particles with the same initial value of x_1.

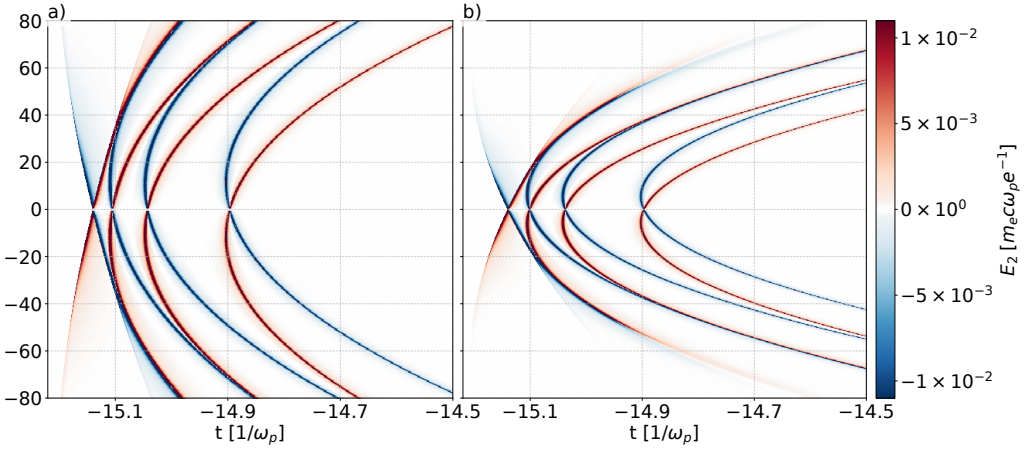

Figure 4.7: Radiation emitted by two of the beam's particles with symmetric initial transverse positions. a) Two particles initailly at $x_1 = 15.05\, c/\omega_p$ and $|x_2| = 3\, c/\omega_p$. b) Two particles initailly at $x_1 = 15.05\, c/\omega_p$ and $|x_2| = 2\, c/\omega_p$.

Furthermore, it is worth noting that the field's intensity with only two radiative particles is about one hundred times smaller than the one obtained with the full beam, which is in agreement with the hypothesis that constructive interference happens mostly for particles in the same vertical slice of the beam, given that with the density distribution of equation (4.2) the beam is expected to have about 200 particles per vertical slice in that region.

The trajectory and radiation of a test particle placed inside the electron beam can provide a deeper insight on the signature left by a particle undergoing betatron motion. Figure 4.10 shows the comparison between a particle undergoing a perfect sinusoidal motion in a vacuum and a particle from the electron beam undergoing betatron motion inside a plasma subject to deceleration. Panels a) and b) display the clear difference between both trajectories: while the period and amplitude of the decelerated particle (in blue) change drastically as time progresses, the particle in a vacuum remains unaffected. This results in visible disparities between the spatiotemporal profiles, as evidenced by Figure 4.10.

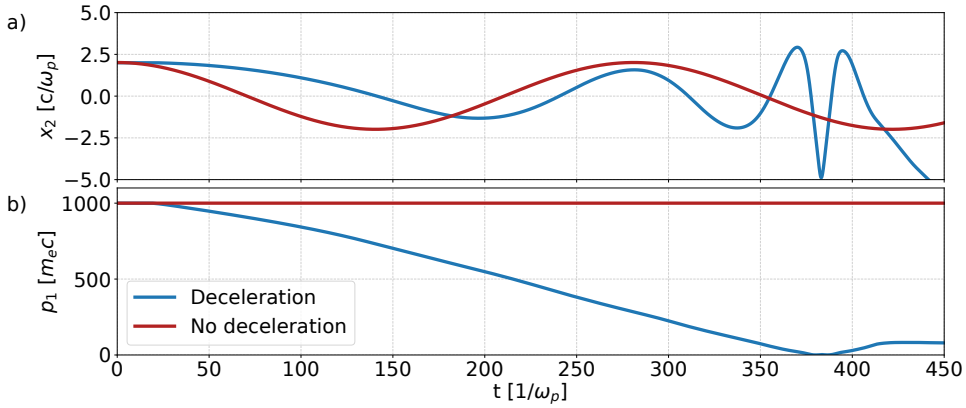

Figure 4.8: Comparison between a particle undergoing a perfect sinusoidal trajectory (no acceleration) and a particle undergoing betatron motion in a plasma (deceleration).

Despite the differences, both profiles contain sequences of positive and negative parabolae, with the peculiarity that all parabolae with a vertex at $\phi > 0$ comprise negative field values, whereas all parabolae with vertex at $\phi < 0$ comprise positive field values. Keeping in mind that each pronounced parabola corresponds to a maximum emission point in the trajectory (*i.e.* the points where the particles velocity is parallel to the direction of observation, $\sim \mathbf{e_{x_1}}$), we arrive to the conclusion that the vertex of each parabola corresponds to the position of the cell that was closer to the particle at the time of emission. It is therefore possible to predict the position of the vertex of each parabola given the trajectory of the particle, as it can be calculated by finding the detector's cell that minimizes the distance, d, to the particle, as illustrated by Figure 4.9 and the following equation:

$$\phi_{\text{vertex}} = \arg\min_{\phi} d(\phi) = \arccos\frac{x_{p1}}{|x_p|}, \qquad t_{\text{vertex}} = t_{\text{ret}} + \frac{R - |x_p|}{c}. \tag{4.3}$$

This prediction is presented in panels a) and b) of Figure 4.10 as a black line. Its agreement with the simulation results is excellent, as it follows the evolution of the parabolae very closely. While this may appear to be a trivial result, it suggests that the inverse operation may be possible, allowing for the reconstruction of the particle's trajectory from the spatiotemporal signature of the radiation it emitted.

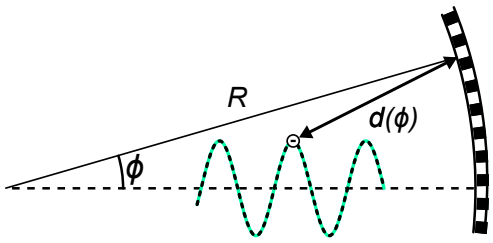

Figure 4.9: Illustration of the function $d(\phi)$. The distance from the particle to the detector is a minimum when the observation vector, $\mathbf{n}$ is parallel to the position vector of the particle $\mathbf{x}$.

Such a study is not in the scope of this work, but may be of major relevance in future studies.

In a sinusoidal trajectory these emission points correspond to the turning points, which are characterized by a strong transverse acceleration (along $\mathbf{e_{x_2}}$) pointing to the x_2 axis, that is, if $x_2 > 0$, $\dot{\boldsymbol{\beta}}$ points downwards, and if $x_2 < 0$, points upwards. This fact has direct implications on the signal of the electric field, as $\mathbf{E} \sim \mathbf{n} \times \dot{\boldsymbol{\beta}} \sim \mathbf{e_{x_1}} \times \dot{\boldsymbol{\beta}}$), and implies that fields corresponding to two consecutive turning points will have opposing signal. This is the main reason why the fields emitted by the full beam are positive for $\phi < 0$ and negative for $\phi > 0$.

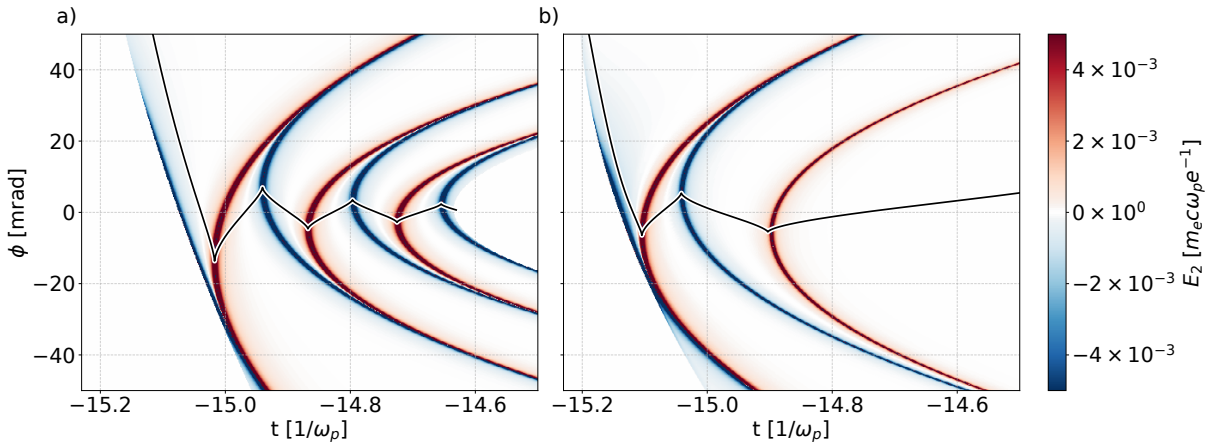

Figure 4.10: Helical trajectory of the particle. Relativistic particle undergoing a circular motion on the x_2x_3 plane while moving forward in the x_1 direction. $\gamma = 100$.

Chapter 5

The effect of macroparticles

This chapter follows the efforts put through in order to bring the simulations results closer to what a real experiment would yield.

Although the PIC algorithm allows for a significant reduction of the operations needed to simulate a plasma, one-to-one simulations are typically out of reach, as actual laboratory experiments such as the ones concerning laser plasma interactions contain a very high number of particles. Therefore, PIC codes like OSIRIS, only simulate a fraction of the plasma's particles using the so-called *macroparticles*.

A macroparticle is the computational way of representing a group of particles, as displayed in Figure 5.1, that are assumed to move with same momentum throughout the simulation, keeping their spatial distribution static over time. This assumption is usually valid in scenarios where the collective effects dominate over the individual motion (*e.g* laser-plasma interaction). Depending on the physical process at study, the number of particles grouped inside a macroparticle should be selected in order to ensure the validity of this approximation.

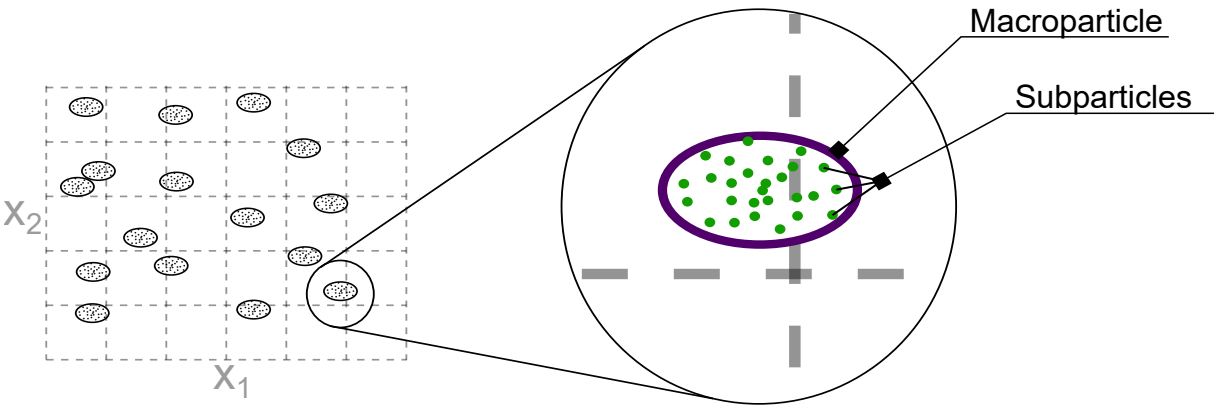

Figure 5.1: Illustration of the macropaticle concept

As it is virtually impossible to determine the spatial distribution of each macroparticle (*i.e.* how the subparticles distributed inside the macroparticle) the radiation diagnostic assumes that all particles are concentrated in the same spot. However, as discussed by Pausch et al. [36], the shape of this distribution may affect the coherence of the emitted radiation. By performing a spectral analysis the authors of that paper determined that the integral of equation (1.3) should include a spatial integration in order to take

the spatial distribution into account. Therefore the radiated spectrum should be given by:

$$\frac{d^2I}{d\omega d\Omega} = \frac{q_e^2}{4\pi^2 c}\left|\int_V \rho(\mathbf{r_0}-\mathbf{r})dV \int_{-\infty}^{\infty} \frac{\mathbf{n}\times[(\mathbf{n}-\boldsymbol{\beta})\times\dot{\boldsymbol{\beta}}]}{(1-\boldsymbol{\beta}\cdot\mathbf{n})^2} e^{i\omega(t_{\text{ret}}-\frac{\mathbf{n}\cdot(\mathbf{r_0}-\mathbf{r})}{c})} dt_{\text{ret}}\right|^2 \tag{5.1}$$

where $\rho(\mathbf{r})$ is the charge density distribution of the particles inside the macroparticle, which can be assumed to be centered around the center of the macroparticle $\mathbf{r_0}$, in this case the spatial integral can be taken as the Fourier transform of the charge distribution, $\mathcal{F}_\rho$:

$$\begin{aligned}\frac{d^2I}{d\omega d\Omega} &= \frac{q_e^2}{4\pi^2 c}\left|\int_{-\infty}^{\infty} \frac{\mathbf{n}\times[(\mathbf{n}-\boldsymbol{\beta})\times\dot{\boldsymbol{\beta}}]}{(1-\boldsymbol{\beta}\cdot\mathbf{n})^2} e^{i\omega(t_{\text{ret}}-\frac{\mathbf{n}\cdot\mathbf{r_0}}{c})} dt_{\text{ret}} \int_V \rho(\mathbf{r}-\mathbf{r_0}) e^{i\omega(t_{\text{ret}}-\frac{\mathbf{n}\cdot\mathbf{r}}{c})} dV\right|^2 \\ &= \frac{q_e^2}{4\pi^2 c}\left|\int_{-\infty}^{\infty} \frac{\mathbf{n}\times[(\mathbf{n}-\boldsymbol{\beta})\times\dot{\boldsymbol{\beta}}]}{(1-\boldsymbol{\beta}\cdot\mathbf{n})^2} e^{i\omega(t_{\text{ret}}-\frac{\mathbf{n}\cdot\mathbf{r_0}}{c})} dt_{\text{ret}}\right|^2 \mathcal{F}_\rho^2(\omega/c)\,.\end{aligned} \tag{5.2}$$

For a point-like macroparticle the charge density may be written as a Dirac-delta function, $\rho = \delta(\mathbf{r}-\mathbf{r_0})$, whose Fourier transform is equal to 1. In this case, the charge distribution has no effect on the amplitude of the emitted, harmonics. However, if the charge density is a discrete set of N particles distributed according to the continuous charge distribution ρ the radiated spectrum would be given by [36]:

$$\frac{d^2I}{d\omega d\Omega} = \frac{q_e^2}{4\pi^2 c}\left|\int_{-\infty}^{\infty} \frac{\mathbf{n}\times[(\mathbf{n}-\boldsymbol{\beta})\times\dot{\boldsymbol{\beta}}]}{(1-\boldsymbol{\beta}\cdot\mathbf{n})^2} e^{i\omega(t_{\text{ret}}-\frac{\mathbf{n}\cdot\mathbf{r_0}}{c})} dt_{\text{ret}}\right|^2 \left[N + \left(N^2-N\right)\mathcal{F}_\rho^2(\omega/c)\right]\,. \tag{5.3}$$

The N factor accounts for the incoherent emission that happens after the shape function cuts-off (for higher frequencies), whereas the (N^2-N) accounts for coherent emission that happens for lower frequencies.

While it is true that it is not possible to determine the exact shape of the simulation's macroparticles one can always assume a generic shape function. In fact one of the most common macroparticle shapes is the so called Cloud in Cell (CIC), which consists in an uniform distribution of subparticles resulting in a rectangular function Π with a given width σ, as shown in the left panel of Figure 5.2. The Fourier transform of this shape function is the sinc function, more specifically: $\mathcal{F}_{\Pi(x)}(\omega) = \sigma/c\,\text{sinc}(\omega\sigma/2c)$ and it is plotted in the right panel of Figure 5.2.

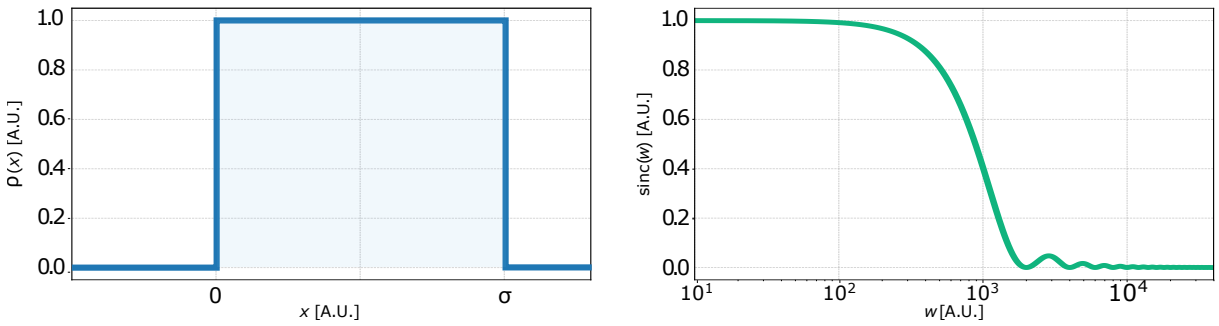

Figure 5.2: Cloud-In-Cell Shape function ($\rho(x)$) and its Fourier transform, the sinc(w) function, plotted in a horizontal log scale.

In order to simulate the effect of the macroparticle shape function on the emitted radiation we

added an extension to the post-processing diagnostic that allowed the user to specify the shape of the macroparticle and number of subparticles to be used in the simulation. This tool's functioning is based on the assumption that a spatial charge distribution results in an equivalent deposition time distribution, that is: if the particles are distributed uniformly along space, then the times at which they will deposit radiation are equally distributed.

For these simulations, we used the sinusoidal trajectory of Figure 3.1 with a slice of spherical detector of radius $R = 10^5\, c/\omega_p$ located in the x_2x_3 plane with azimuthal angle $\phi = 0$ and polar angle θ ranging from $\pi/2 - 0.08$ to $\pi/2 + 0.08$ rad with 512 spatial cells that accepted radiation from $t = R/c + 0.01\,\omega_p^{-1}$ to $t = R/c + 4\,\omega_p^{-1}$ with 131072 temporal cells. We added a CIC shape to the macroparticles, which were composed of 128 subparticles and then varied the width of the distribution from $\sigma = 10^{-7}\, c/\omega_p$ to $\sigma = 2 \times 10^{-3}\, c/\omega_p$.

The simulated electric field was transformed into a frequency-angular spectrum by means of an FFT and then integrated along the angular direction. Similarly to what happened in section 3.1, the produced frequency spectrum was a not a smooth curve, but set of densely distributed discrete peaks enveloped by the theoretical expression on Equation (3.6). With the aim of retrieving the envelope from the simulation's results we ran a peak detection algorithm together with a smoothing Savitzky-Golay filter [37]. The resulting spectra are displayed on the left panel of Figure 5.3. Even though the spectrum of this kind of radiation decays naturally for higher frequencies, it is possible to verify that when the macroparticle becomes wider (higher σ), this decay happens earlier as the spectrum is modulated by the sinc shape function. Furthermore, the characteristic ripples of this shape function that could be observed in Figure 5.2 also appear on the spectra for higher σ.

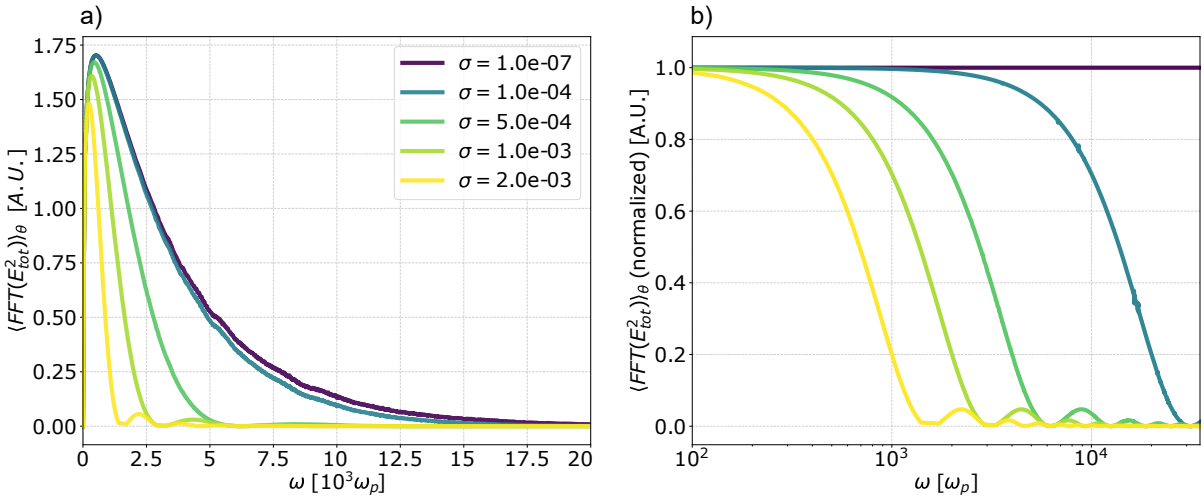

Figure 5.3: Comparison between the spectra emitted by macroparticles with different sizes. a) Direct comparison of the spectra. b) Ratio between each spectra and the spectrum obtained for a point-like macroparticle.

By normalizing each spectrum to the spectrum generated with $\sigma = 0$ we were able to obtain the shape function for each σ. The results are plotted in the right panel on Figure 5.3 and it is possible to see that in the available range of frequencies, the shape functions clearly match the expected sinc function. These shape functions resemble the intensity response of low-pass filters: approximately constant for frequencies below the cut-off frequency and rapidly decreasing for frequencies near the

cut-off frequency. In these radiation emission phenomena, this filtering occurs due to coherence effects: a macroparticle with a given size emits coherent radiation if the wavelength of the radiation is larger than its typical size and emits incoherent radiation if the wavelength of the radiation is smaller than its typical size.

The mathematical framework developed by R. Paush allows for an easy understanding of why the spectrum's intensity should decay for higher frequencies. However, some more physical insight can be given by the spatiotemporal picture of the emitted radiation. Figure 5.4 shows the difference between the spatiotemporal signature of a macroparticle with $\sigma = 10^{-7}\, c/\omega_p$ and a macroparticle with $\sigma = 10^{-2}\, c/\omega_p$. With a smaller macropaticle the radiation is much more intense, with shorter pulses (temporally). The opposite happens for larger macroparticles, as the radiation from each subparticle is no longer focused on the same time slot which also leads to destructive interference. This fact is evidenced by the lineout on the right panel of Figure 5.4, where the strong pulse generated by the small macroparticle becomes broader when the macroparticle becomes wider with a much longer and less steep transition between the positive and negative parts of the pulse caused by the interference between the singular pulses of each subparticle.

For these results we show the unnormalized value of the electric which was obtained by using the following conversion factor for a plasma of density $n_0 = 1.6 \times 10^{-19}[cm^{-3}]$:

$$\mathbf{E}\,[\text{GV/cm}] = 9.613 \times 10^{-10}\mathbf{E}'[m_e c\omega_p e^{-1}]n_0[\text{cm}^{-3}] \tag{5.4}$$

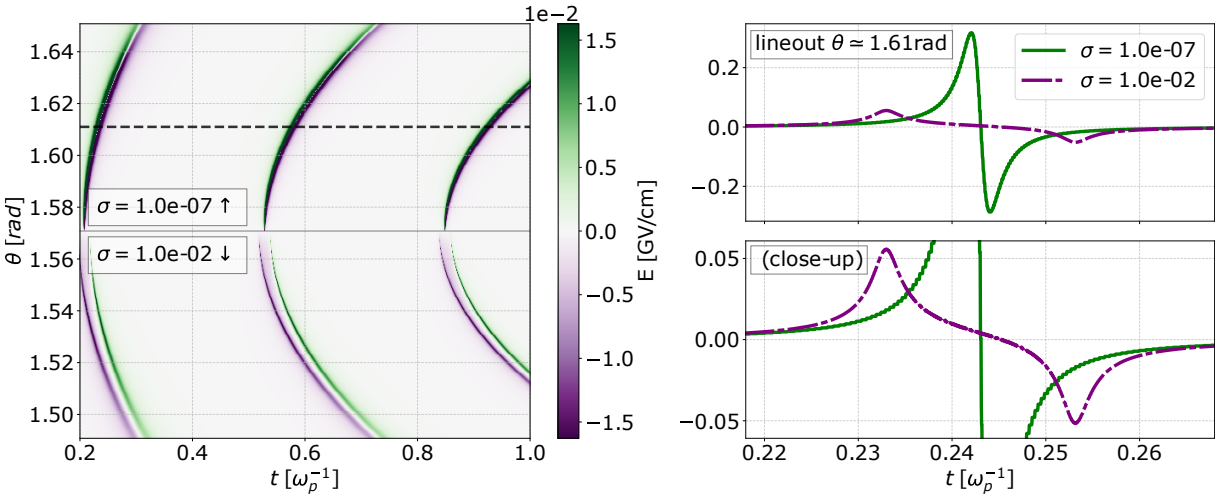

Figure 5.4: Comparison between the spatiotemporal profiles of the radiation emitted by two types of macroparticles. The left plot shows the two complementary halves of the full detector. The lineout is shown on the right panels, featuring a close-up.

The fact that the shape function corresponds to the quotient of the spectrum of the radiation obtained with larger macroparticles and the spectrum obtained with a point particle seems to suggest that the addition of subparticles to the macroparticle acts as a filter, leaving out the high-frequency components. In this way it may be possible to obtain the correct spatiotemporal signature from the point particle's signature through Fourier filtering. However, apart from not having been fully tested, this operation requires strong assumptions about the shape of the macroparticle, therefore this issue requires further

analysis.

An interesting test that could shed some light into this subject would be running the plasma acceleration simulation from the previous chapter with some minor tweaks. As the goal is to assess how the results vary with the addition of more particles, it could be interesting to select a small portion of the beam as a radiative species and increase the number of simulation particles in that region to a point where coherence effects (or lack there of) would start to show.

Chapter 6

Conclusions

The radiation diagnostic for OSIRIS was successfully implemented, benchmarked and tested in several scenarios, including production runs. This tool, which was later named RaDiO, offers the users two distinct ways of obtaining the spatiotemporal profile of radiation emitted by charged particles: either by analyzing previously obtained trajectories with the post processing code or directly inside a PIC simulation with the code's incorporation into OSIRIS.

Both versions were implemented as parallel codes, using both shared and distributed memory parallelization, allowing users to run this tool in the world's most powerful supercomputers. The code was put through scaling and performance tests in massive parallel systems, yielding little parallel efficiency loss even at high core counts albeit with a somewhat larger than expected computational cost for a detector with a large number of spatial cells, leaving space for future improvements.

Furthermore, the code was benchmarked against theoretical predictions and other well established spectral radiation codes in well known scenarios, providing solid, trustworthy results, which allowed for production runs to be performed with a high level of confidence.

RaDiO was used to probe the previously unexplored spatiotemporal features of radiation emitted in PWFA scenarios, which led to two interesting conclusions:

i) It may be possible to further accelerate particles located far away with the radiation emitted in PWFA.

ii) It may be possible to infer some properties of the original driving beam by assessing the periodicity of typical structures of radiation.

Both these topics require deeper examination but the analysis presented here may lay the groundwork for future studies.

Finally, the size of the macroparticle was shown to affect the radiated spectrum, as the intensity of the emitted radiation decreases for wavelengths of the order of the size of the macroparticle caused by a loss of coherence for higher frequencies. The corrected spectrum can be obtained from the original one by a multiplication with a shape function, which seems to imply that the corrected spatiotemporal profile can be obtained through some sort of Fourier filtering. This claim has not yet been tested, but additional simulations clarify the process.

The future work concerning this diagnostic can be split in development and simulation tasks From the development side, the code and its documentation still need to be included in the official OSIRIS release so that they can be easily distributed. Moreover, there are some interesting features that could be added to the code:

i) **Vector parallel computing**. Study the possibility of applying an additional level of parallelizatiion to the code;

ii) **Particle selection**. Enable the selection of the sub group of particles from a radiative species that will radiate;

iii) **Polarization diagnostic**. Obtain the polarization of the emitted light from the components of the EM fields.

Apart from the scenarios discussed above, there are other setups in which the spatiotemporal properties of radiation are crucial. For example, HHG is a highly non-linear phenomenon that can be enhanced with spatiotemporally structured beams, which can be thoroughly studied using RaDiO.

Overall, the tool developed on this thesis provides solid, trustworthy results, allowing for the study of previously unexplored properties of radiation in highly relevant scenarios.

Bibliography

[1] W. J. Percival, L. Samushia, A. J. Ross, C. Shapiro, and A. Raccanelli. Redshift-space distortions. *Philosophical Transactions of the Royal Society of London Series A*, 369:5058–5067, Dec. 2011. doi: 10.1098/rsta.2011.0370.

[2] L. Allen et al. Orbital angular momentum of light and the transformation of laguerre-gaussian laser modes. *Phys. Rev. A*, 45:8185–8189, Jun 1992. doi: 10.1103/PhysRevA.45.8185.

[3] F. Tamburini, B. Thidé, G. Molina-Terriza, and G. Anzolin. Twisting of light around rotating black holes. *Nature Physics*, 7:195 EP –, Feb 2011. URL http://dx.doi.org/10.1038/nphys1907.

[4] K. Nishikawa and M. Wakatani. *Plasma Physics: Basic Theory with Fusion Applications (Springer Series on Atomic, Optical, and Plasma Physics)*. Springer, 2000. ISBN 354065285X. URL https://www.amazon.com/Plasma-Physics-Applications-Springer-Optical/dp/354065285X?SubscriptionId=AKIAIOBINVZYXZQZ2U3A&tag=chimbori05-20&linkCode=xm2&camp=2025&creative=165953&creativeASIN=354065285X.

[5] S. W. Hell and J. Wichmann. Breaking the diffraction resolution limit by stimulated emission: stimulated-emission-depletion fluorescence microscopy. *Opt. Lett.*, 19(11):780–782, Jun 1994. doi: 10.1364/OL.19.000780. URL http://ol.osa.org/abstract.cfm?URI=ol-19-11-780.

[6] P. Emma et al. First lasing and operation of an Angstrom-wavelength free-electron laser. *Nature Photonics*, 4:641–647, Aug 2010. doi: 10.1038/nphoton.2010.176.

[7] E. Esarey, C. B. Schroeder, and W. P. Leemans. Physics of laser-driven plasma-based electron accelerators. *Rev. Mod. Phys.*, 81:1229–1285, Aug 2009. doi: 10.1103/RevModPhys.81.1229.

[8] F. Albert et al. Laser wakefield accelerator based light sources: potential applications and requirements. *Plasma Physics and Controlled Fusion*, 56(8):084015, 2014. doi: 10.1088/0741-3335/56/8/084015.

[9] E. Esarey, B. A. Shadwick, P. Catravas, and W. P. Leemans. Synchrotron radiation from electron beams in plasma-focusing channels. *Phys. Rev. E*, 65:056505, May 2002. doi: 10.1103/PhysRevE.65.056505. URL https://link.aps.org/doi/10.1103/PhysRevE.65.056505.

[10] G. Gariepy, J. Leach, K. T. Kim, T. J. Hammond, E. Frumker, R. W. Boyd, and P. B. Corkum. Creating high-harmonic beams with controlled orbital angular momentum. *Phys. Rev. Lett.*, 113:

153901, Oct 2014. doi: 10.1103/PhysRevLett.113.153901. URL https://link.aps.org/doi/10.1103/PhysRevLett.113.153901.

[11] J. M. Dawson. Particle simulation of plasmas. *Rev. Mod. Phys.*, 55:403–447, Apr 1983. doi: 10.1103/RevModPhys.55.403.

[12] K. Yee. Numerical solution of initial boundary value problems involving maxwell's equations in isotropic media. *IEEE Transactions on Antennas and Propagation*, 14(3):302–307, May 1966. doi: 10.1109/TAP.1966.1138693.

[13] R. A. Fonseca et al. *OSIRIS: A Three-Dimensional, Fully Relativistic Particle in Cell Code for Modeling Plasma Based Accelerators*, pages 342–351. Springer Berlin Heidelberg, Berlin, Heidelberg, 2002. ISBN 978-3-540-47789-1. doi: 10.1007/3-540-47789-6_36.

[14] S. H. Glenzer, W. E. Alley, K. G. Estabrook, J. S. De Groot, M. G. Haines, J. H. Hammer, J.-P. Jadaud, B. J. MacGowan, J. D. Moody, W. Rozmus, L. J. Suter, T. L. Weiland, and E. A. Williams. Thomson scattering from laser plasmas. *Physics of Plasmas*, 6(5):2117–2128, 1999. doi: 10.1063/1.873499. URL https://doi.org/10.1063/1.873499.

[15] J. D. Jackson. *Classical Electrodynamics*, chapter 14. Wiley, 3rd ed. edition, 1999.

[16] S. Corde et al. Femtosecond x rays from laser-plasma accelerators. *Rev. Mod. Phys.*, 85:1–48, Jan 2013. doi: 10.1103/RevModPhys.85.1.

[17] J. L. Martins, S. F. Martins, R. A. Fonseca, and L. O. Silva. Radiation post-processing in PIC codes. *Proc.SPIE*, 7359, 2009. doi: 10.1117/12.820736.

[18] R. Pausch et al. How to test and verify radiation diagnostics simulations within particle-in-cell frameworks. *Nuclear Instruments and Methods in Physics Research Section A: Accelerators, Spectrometers, Detectors and Associated Equipment*, 740:250–256, 2014. doi: 10.1016/j.nima.2013.10.073.

[19] S. Kneip et al. Bright spatially coherent synchrotron X-rays from a table-top source. *Nature Physics*, 6:980–983, Oct 2010. doi: 10.1038/nphys1789.

[20] S. Kneip et al. X-ray phase contrast imaging of biological specimens with femtosecond pulses of betatron radiation from a compact laser plasma wakefield accelerator. *Applied Physics Letters*, 99 (9):093701, 2011. doi: 10.1063/1.3627216.

[21] H. Burau et al. PIConGPU: A Fully Relativistic Particle-in-Cell Code for a GPU Cluster. *IEEE Transactions on Plasma Science*, 38(10):2831–2839, Oct 2010. doi: 10.1109/TPS.2010.2064310.

[22] E. Esarey, S. K. Ride, and P. Sprangle. Nonlinear Thomson scattering of intense laser pulses from beams and plasmas. *Phys. Rev. E*, 48:3003–3021, Oct 1993. doi: 10.1103/PhysRevE.48.3003.

[23] A. Sainte-Marie. Diagnostics for the transient-radiative field in PIC simulations. Presentation, Sep. 2016.

[24] A. Reboul-Salze. Modelling ultra-high frequency x-ray emission in particle-in-cell codes. Technical report, Instituto Superior Tecnico, July 2017.

[25] J. Wang et al. 3D electromagnetic plasma particle simulations on a MIMD parallel computer. *Computer Physics Communications*, 87(1):35–53, 1995. doi: 10.1016/0010-4655(94)00167-Z.

[26] B. M. Kincaid. A short-period helical wiggler as an improved source of synchrotron radiation. *Journal of Applied Physics*, 48(7):2684–2691, 1977. doi: 10.1063/1.324138.

[27] SuperMUC petascale system. `www.lrz.de/services/compute/supermuc/systemdescription/`. Accessed: 2018-10-14.

[28] Top500 Supercomputer Sites. `www.top500.org`. Accessed: 2018-10-14.

[29] R. A. Fonseca, J. Vieira, F. Fiuza, A. Davidson, F. S. Tsung, W. B. Mori, and L. O. Silva. Exploiting multi-scale parallelism for large scale numerical modelling of laser wakefield accelerators. *Plasma Physics and Controlled Fusion*, 55(12):124011, 2013. URL `http://stacks.iop.org/0741-3335/55/i=12/a=124011`.

[30] L. Cranberg. The initiation of electrical breakdown in vacuum. *Journal of Applied Physics*, 23(5): 518–522, 1952. doi: 10.1063/1.1702243. URL `https://doi.org/10.1063/1.1702243`.

[31] T. C. collaboration. Performance of cms muon reconstruction in pp collision events at sqrts = 7 tev. *Journal of Instrumentation*, 7(10):P10002, 2012. URL `http://stacks.iop.org/1748-0221/7/i=10/a=P10002`.

[32] T. Tajima and J. M. Dawson. Laser electron accelerator. *Phys. Rev. Lett.*, 43:267–270, Jul 1979. doi: 10.1103/PhysRevLett.43.267. URL `https://link.aps.org/doi/10.1103/PhysRevLett.43.267`.

[33] I. Kostyukov, S. Kiselev, and A. Pukhov. X-ray generation in an ion channel. *Physics of Plasmas*, 10(12):4818–4828, 2003. doi: 10.1063/1.1624605. URL `https://doi.org/10.1063/1.1624605`.

[34] J. Vieira, C.-K. Huang, W. B. Mori, and L. O. Silva. Polarized beam conditioning in plasma based acceleration. *Phys. Rev. ST Accel. Beams*, 14:071303, Jul 2011. doi: 10.1103/PhysRevSTAB.14.071303. URL `https://link.aps.org/doi/10.1103/PhysRevSTAB.14.071303`.

[35] P. Chen, J. M. Dawson, R. W. Huff, and T. Katsouleas. Acceleration of electrons by the interaction of a bunched electron beam with a plasma. *Phys. Rev. Lett.*, 54:693–696, Feb 1985. doi: 10.1103/PhysRevLett.54.693. URL `https://link.aps.org/doi/10.1103/PhysRevLett.54.693`.

[36] R. Pausch, A. Debus, A. Huebl, U. Schramm, K. Steiniger, R. Widera, and M. Bussmann. Quantitatively consistent computation of coherent and incoherent radiation in particle-in-cell codes - a general form factor formalism for macro-particles. *Proc. EAAC*, 2017.

[37] A. Savitzky and M. J. E. Golay. Smoothing and differentiation of data by simplified least squares procedures. *Anal. Chem.*, 36(8):1627–1639, Jul 1964. ISSN 0003-2700. doi: 10.1021/ac60214a047. URL `https://doi.org/10.1021/ac60214a047`.

Appendix A

Input File Examples

A.1 Post-processing code

```
&input
filename = "ebeam-tracks.h5"

track_dim=2 !track_dimension (1,2 or 3)

ec_opt=2 ! 2 => Far-filed approximation // 1 => Exact calculation

charge=-1  !particle charge

!lower and upper bounds of the detector: (t,x1,x2,x3)
dmin(:)=-20.01 ,1.47078, -0.0, 100000.
dmax(:)=-5,  1.6707963267948966, 0.2,  100001.
nf(:)=8192,512,1,1   !number of cells in each direction

decomp="cart"  !other option is "sphe" for spherical decomposition

comps(:)=.True.,.True.,.True.,.False.,.False.,.False.
!E(theta,phi,r),B(theta,phi,r) spherical
!E(x,y,z),B(x,y,z) for cartesian

nsp=128    !number of sub particles (for the macroparticle calculation)
mpr=1e-2   !size of the macroparticle

outfile="sphel.h5"   !output file name
/    !This final slash is indispensable
```

A.2 OSIRIS module (run-time code)

```
... ! Remaining  OSIRIS input file
spherical !type of detector (the other option is "cart")
{
nf(:)=163840,256,1,1,                    !number of cells
dmin(:)=-12.1,1.510796326,-0.,1000000,  !detector bounds
dmax(:)=-10.8,1.57079328,0.2,1000001,
decomp="cart",                           !field decomposition
apprx=.True.,                            !far-field approximation
comps(:)=.True.,.True.,.True.,.False.,.False.,.False.,
ndump_fac_det=390,                       !dump frequency of the detector
}

species !radiative species properties always come after the detector
{
  name = "ebeam",
  num_par_max = 500000,
  rqm = -1.,
  num_par_x(1:2) = 1, 1,
  init_fields = .true.,
  q_real=-1.,
}
... ! Remaining  OSIRIS input file
```

The dump frequency determines the rate at which the detector data is written to disk.